Phase and Interface Design in Potential Earth-Abundant Multi-Component Photocatalysts

David Llorens Rauret

Phase and Interface Design in Potential Earth-Abundant Multi-Component Photocatalysts

David Llorens Rauret

Project in Inorganic Nanomaterials
2022
30 hp

Supervisor:
Michael Seifner
Centre for Analysis and Synthesis

Popular Science Summary

Green hydrogen is a potential candidate to be one of the future energy sources. It is a non-pollutant, sustainable and renewable fuel obtained *via* clean ways from water. However, current ways of producing hydrogen in a sustainable process are inefficient and expensive; therefore, more extensive efforts should be made to progress in green hydrogen production. The process of generating hydrogen from water and solar light using a photocatalyst is called photocatalysis. The photocatalyst is a material that increases the rate of a chemical reaction, and its design is the focus of this work.

An essential factor for efficiently promoting chemical reactions *via* light is the photocatalyst's surface interacting with the reactants. Nanoparticles, structures a million times smaller than a metre, have a large surface-volume ratio and are therefore ideal catalysts. There is a wide range of materials used in photocatalysis. However, recent developments highlight the need to create sustainable and efficient materials to progress in this field. Transition metal phosphides are known for their excellent performance in photocatalysis due to their exceptional electronic and physical properties. Moreover, it is well-known in the literature that combining nanomaterials can drastically improve the performance of photocatalysts.

This thesis focuses on the controlled formation of nickel and copper-based phosphides. For this purpose, we created nanoparticles containing the two metals and exposed them to controlled flows of phosphine gas, resulting in the formation of transition metal phosphides. As their photocatalytic activity depends on the shape and structure of the nanoparticles, we investigated those properties in an electron microscope. Specifically, we studied the effect of different parameters, such as temperature and precursor flow, on the shape and structure of the nanoparticles. The obtained results provide a basic understanding of the nickel-copper-phosphorus system and highlight ways to design future photocatalysts with the potential to progress in clean energy production.

Abstract

Transition metal phosphides are low-cost, earth-abundant semiconductors with promising properties for photocatalysis, including water-splitting. When combined with other semiconductors or noble metals in nanoparticles, their photocatalytic performance can be drastically enhanced. Currently, significant research efforts are aiming to explore the facet and interface evolution and the correlation with their photocatalytic activity. However, the controlled formation of multi-component nanoparticles is not trivial due to the little knowledge of their formation mechanisms.

This thesis aims to provide a fundamental understanding of the Ni-Cu-P nano-system, including its dependence on the synthesis parameters. For that purpose, Ni-Cu nanoparticles reacting with phosphine were investigated under growth conditions using an environmental transmission electron microscope with an integrated gas handling system. The used setup allowed the assessment of dynamic processes during the synthesis and detailed characterisation of the products using power spectra of the acquired high-resolution transmission electron microscopy images/movies and energy dispersive X-ray spectroscopy. The reaction of Ni-Cu nanoparticles with a relatively low phosphine flow yielded nanoparticles containing the Ni_5P_4 and Cu_3P phases, whereas higher phosphine flows helped stabilise the Ni_5P_4 and CuP_2 phases. Furthermore, annealing under different conditions enabled the nanoparticles' rearrangement, including forming a single ternary phase and its separation.

This work provides a starting point for studying the Ni-Cu-P nano-system and demonstrates the impact of different parameters, such as the precursor flow and temperature, on forming different phases and their arrangement. Therefore, the obtained results will help progress in developing and designing sustainable photocatalysts to produce clean energy efficiently.

Keywords: facet control, in-situ TEM, nanoparticle heterostructures, phase transformation, transition metal phosphides.

Acknowledgements

I would like to thank my supervisor Michael for introducing me to the research world and everything he has taught me during these months. Despite the significant setback in completing the thesis, he has always transmitted optimism and maintained confidence in finishing this project, which encouraged me to be optimistic and confident too.

I also want to thank Kimberly for giving me the opportunity to do my thesis in Lund and learn how to be part of a research group. These last months, I saw how research within a university works in first person.

I wish to extend my thanks to all the members of the Inorganic NanoMaterials group: Daniel, Mikelis, Robin, Sebastian, Simon, and Tianyi, for all I have learnt from them in the weekly group meetings (and for the cakes). Moreover, I want to express my gratitude to Pau for the nanoparticle deposition. I would also like to thank Ofentse and Henrik for creating such a nice working environment in the office.

Finally, I would also like to thank my friends and family who supported me. And to Elvira, for listening to me practising again and again for the presentations.

List of abbreviations

PC, photocatalytic

HER, hydrogen evolution reaction

OER, oxygen evolution reaction

VB, valence band

CB, conduction band

NHE, normal hydrogen electrode

NP, nanoparticle

LSPR, localized surface plasmon resonance

TMP, transition metal phosphides

TEM, transmission electron microscope

DMA, differential mobility analyser

MEMS, microelectromechanical systems

HRTEM, high-resolution transmission electron microscopy

STEM, scanning transmission electron microscopy

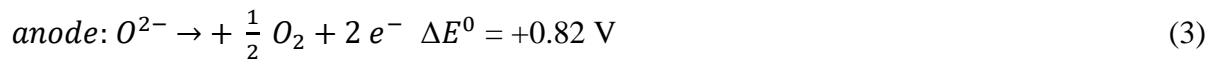**EDS**, energy dispersive X-ray spectroscopy
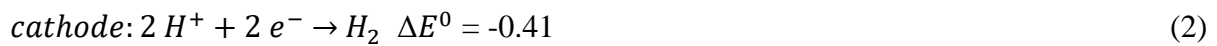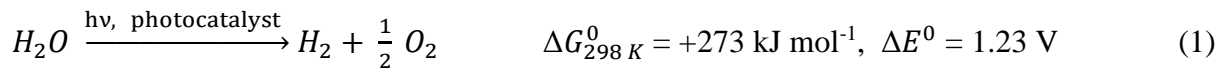
FFT, fast Fourier transform

Contents

1 Introduction

The recent developments in the global energy crisis and the European Commission's commitments to reduce greenhouse gas emissions to at least 55% by 2030[1] highlight the urgency of creating non-pollutant, sustainable, and renewable energy sources. Green hydrogen, generated exclusively by renewable energy sources such as solar or wind energy in combination with water, is a promising environmentally friendly substitute for traditional fossil fuels. Currently, the high costs of green hydrogen production prevent progress in reaching the defined goals. In 2020, 76% of the global production was provided from natural gas *via* steam methane reforming, 22% from coal gasification, and only 2% from water.[2]

Photoelectrochemical and photocatalytic (PC) water-splitting are approaches for generating green hydrogen. Equation 1 reveals the chemical reaction representing the addressed process. It allows the conversion of earth-abundant water by solar light to chemical energy in the form of H_2 and O_2 using a catalyst.

$$H_2O \xrightarrow{h\nu,\ photocatalyst} H_2 + \frac{1}{2} O_2 \qquad \Delta G^0_{298\ K} = +273 \text{ kJ mol}^{-1},\ \Delta E^0 = 1.23 \text{ V} \tag{1}$$

$$cathode: 2\,H^+ + 2\,e^- \rightarrow H_2 \quad \Delta E^0 = \text{-0.41} \tag{2}$$

$$anode: O^{2-} \rightarrow + \frac{1}{2} O_2 + 2\,e^- \quad \Delta E^0 = +0.82 \text{ V} \tag{3}$$

However, H_2 and O_2 need to be spatially separated to prevent the explosive backward reaction for the safe implementation of the addressed approaches.[3] For this reason, in photoelectrochemical water-splitting, each of the semi-reactions, the hydrogen evolution reaction (HER, Equation 2) and the oxygen evolution reaction (OER, Equation 3), is performed in a different half-cell. Ion-exchange membranes or ion-permeable separators connect the half-cells.[4,5] In PC water-splitting, the generated gases are separated downstream by gas separation systems.[6] The generated hydrogen can be stored and transported, making it an interesting energy carrier for the industry. H_2 exhibits higher heating values than most fuels. However, its lower energy density results in the drawback that bigger tanks are required for storage than those currently used for fossil fuels.[7] Moreover, H_2 can weaken metals (H_2 embrittlement), and its capability to escape through many materials due to its small molecule size is a significant challenge for H_2 storage.[7,8]

An efficient photocatalyst is essential for implementing Equation 1 *via* a PC process. The photocatalyst is a semiconductor whose role is to initiate and accelerate the chemical reaction by offering charge carriers. The mechanism by which charge carriers are generated in a semiconductor by light irradiation with energies equal to or higher than the bandgap energy of the semiconductor is revealed in Figure 1. The absorption process leads to the excitation of electrons to the valence band (VB), leaving a positively charged hole in the conduction band (CB). Electrons and holes can rapidly recombine in bulk or on the surface of the photocatalyst, releasing energy in the form of heat or photons. However, the electrons/holes that diffuse to the photocatalyst surface without recombination are capable of reducing/oxidizing reactants adsorbed to the photocatalyst surface.[9] Consequently, the efficient separation of electron-hole pairs and the charge carrier diffusion are essential aspects that must be considered for designing photocatalysts.
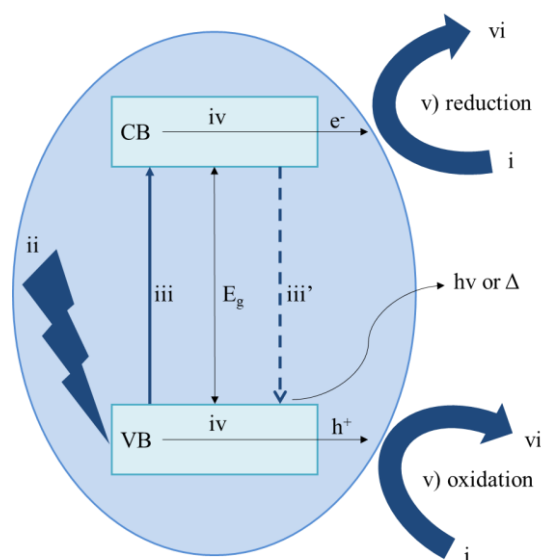

Figure 1. Schematic diagram of the charge carrier separation mechanism in a semiconductor. i) Adsorption of reactants. ii) Absorption of photons with equal or higher energy than the semiconductor's bandgap energy (E_g). iii) Transition of electrons from VB to CB. iii') Recombination of charge carriers yielding heat or photons. iv) Transport of electrons (e^-) and holes (h^+) towards the surface. v) Redox reactions. vi) Desorption of the products.

Semiconductors with favourable bandgaps and charge carrier transport properties are ideal candidates for the role of a photocatalyst.[10] Since discovering TiO_2 photocatalysed water-splitting in 1972,[11] research on semiconductors for PC applications, like pollutant degradation,[12–14] CO_2 reduction,[14–16] or N_2 fixation,[15,17,18] has been intensified. Metal oxides, including ZnO,[10,19] Fe_2O_3,[14,20] WO_3,[13,21] and the already mentioned TiO_2,[16,17,22–31] as well as

chalcogenides[12,32–34] and nitrides[18,33,35] have proven their potential to progress in this research field. Currently, there are huge efforts to expand the range of earth-abundant materials with the potential of achieving efficient water-splitting.[5,36,37]

For efficient hydrogen production, the CB minimum of the semiconductors should be more negative than the HER potential (H^+/H_2, 0 V *versus* the Normal Hydrogen Electrode (NHE) at pH 0). Analogously, the VB maximum should be more positive than the OER potential (O_2/H_2O, +1.23 V *versus* the NHE at pH 0) for efficient oxygen generation.[8,26] In other words, a water-splitting photocatalyst should theoretically have a bandgap energy greater than 1.23 eV and suitable CB and VB energy levels. However, in reality, slightly higher potentials are needed to achieve efficient water-splitting due to the high activation energies required to overcome the kinetic energy barriers.[38–40] In addition, the semiconductor should ideally have a bandgap energy of less than 2.0-2.2 eV to efficiently convert water into H_2 and O_2 by using a large fraction of the solar light spectrum as energy input.[25,41] Higher bandgap energies would result in the sole absorption of radiation in the ultraviolet region of the solar light spectrum. For instance, TiO_2 is only capable of absorbing 5% of the solar light due to its large bandgap (3.0-3.2 eV).[26]

It is worth mentioning that the band structure is not the only aspect that must be considered when designing an efficient photocatalyst. The reagent's adsorption/activation and product's desorption are facet-dependent, and surface terminations play an essential role in water-splitting.[42,43] Therefore, depending on the available surface facets and their atomic arrangement, the properties of the semiconductor can vary, and the overall PC performance can improve.[44] For instance, Cu_2O {110} and {111} facets terminated by Cu atoms show higher PC activity for methyl orange degradation due to Cu atoms' vital role in interacting with the involved supplied species.[45] In general, photocatalysts should have neither too weak nor too strong free energy of reagents adsorption. Weak adsorption may prevent the reaction, and too strong adsorptions could poison the catalyst since all the active sites were occupied.[43,46]

It is well-known in the literature that the proper selection of crystal facets can enhance the PC activity of semiconductors. For instance, the anatase TiO_2 {101} facet, which is the thermodynamically most stable TiO_2 facet,[24] shows the best PC activity in HER,[31] whereas the {001} facet shows higher activity in toxic pollutant degradation.[23] In another example, anatase TiO_2 nanoparticles (NPs) with {111} facets exhibited a significantly higher PC activity in the HER than those with {010}, {101}, and {001} facets.[47] The identity of the facets exposed to

the reactants can affect the PC performance in different ways, such as the facet-dependent 1) adsorption and activation of reactants on the surface,[28] 2) electronic band structure,[47] and 3) accumulation of photogenerated electrons and holes, favouring specific reactions.[48] By increasing the fraction of high activity facets in mono-component semiconductors, highly efficient photocatalysts for a particular chemical reaction can be developed.[42]

Commonly, mono-component photocatalysts with the desired surface facets are synthesised by solution-based synthesis approaches. Thermodynamically controlled syntheses usually result in the formation of facets with low surface energies. Consequently, this form of control usually leads to fewer high-index facets due to their higher surface energies. On the other hand, kinetically controlled syntheses preserve facets with low growth rates, as those with higher rates disappear.[49] By altering parameters such as the reagents' starting concentration, solvent selection, reaction time, and temperature, growth kinetics can be manipulated.[24,50,51] Therefore, thermodynamically unfavourable facets can be formed, allowing the facet-design of NPs.[52] It should be mentioned that the balance between thermodynamics and kinetics must be considered for a controlled surface facet design.[42]

One of the most common synthesis strategies for facet-engineering includes capping agents,[42,51,53] such as surfactants, polymers, or inorganic ions, that are adsorbed to certain facets and suppress their growth by reducing their surface energy or selectively blocking the surfaces. By, *e.g.*, adjusting the capping agent's concentration, the growth of different facets can be rationally controlled.[42] Moreover, capping agents can help create stable NP suspensions by avoiding strong interactions between the particles due to electrostatic and steric stabilisation, which is beneficial for photocatalysis.[54] Nonetheless, capping agents usually remain adsorbed on the facets even after purification and can affect the PC activity by hindering the adsorption and activation of reagents. This can significantly affect the PC activity and highlights the importance of characterising the photocatalysts properly after the synthesis and purification steps to guarantee reliable PC activity measurements.[42] In addition, the capping agents' removal can alter the facet evolution of NPs and initiate the formation of oxide layers which might negatively affect the stability and properties of the photocatalyst.[53,55]

Another synthetic approach to designing NP crystal facets is selective etching, which is based on selectively removing specific NP facets. Due to the atomic and bond arrangement, the etching rates of an extensive range of potential etching reagents can vary in different crystallographic directions, leading to particular NP shapes.[56] The etching rates can also be

influenced by the temperature, solvent selection, and etching time.[57] Additionally, selective etching can be performed using protecting agents that adsorb on certain nanocrystal facets subsequently protected from the etching reagents. As a result, only the unprotected facets are etched, and the desired facets remain.[58]

Multi-component nanostructures, including the combination of semiconductors with other semiconductors or noble metals, have been developed in the last years to improve the performance of photocatalysts. The advantage of such structures originates in two different aspects: 1) the extension of the light absorption range and 2) the efficient separation of electron-hole pairs preventing their recombination.

By coupling small bandgap semiconductors (<1 eV) with large bandgap semiconductors (>1 eV),[59] it is possible to achieve electron-hole pair separation using longer wavelengths, shifting or extending the light absorption to the visible region.[10] The type of the semiconductor-semiconductor heterojunction must be considered an important aspect of achieving efficient charge carrier separation. In general, the interface between two semiconductors (A and B) can be classified into three types (Figure 2): 1) straddling gap (type 1), 2) staggered gap (type 2), and 3) broken gap (type 3).[60] In the type 1 heterojunction, the CB/VB of A is higher/lower than the corresponding band of B. Consequently, both electrons and holes accumulate in B, not allowing an efficient charge carrier separation. In the type 2 heterojunction, both the CB and the VB of A are higher than those of B. Hence, the photogenerated electrons will accumulate in B and the holes in A. Therefore, the charge-carrier pairs can be spatially separated. Finally, in the type 3 heterojunction, the bandgap regions of the two semiconductors do not overlap, making electron-hole pair separation impossible. Consequently, type 2 heterojunctions are the most efficient for electron-hole pair separation and, therefore, promising for enhancing the PC performance.
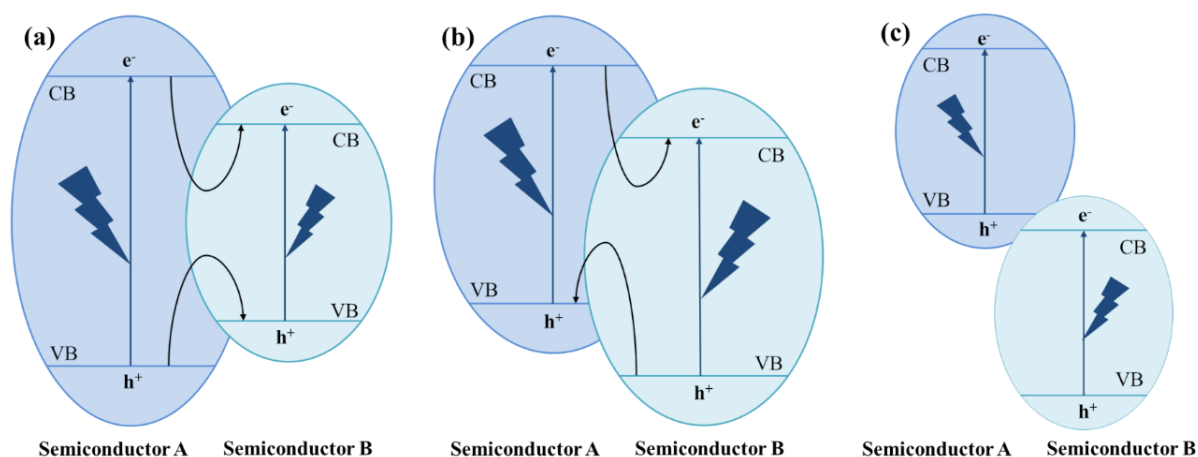
Figure 2. Schematic diagrams of the three different band alignments for semiconductor heterojunctions: a) straddling gap (type 1), b) staggered gap (type 2), and 3) broken gap (type 3).

Another possibility to achieve higher PC performances is the coupling of semiconductors with noble metals, such as Au or Ag, due to the plasmonic effect. The plasmonic energy transfer from the metal to the semiconductor extends the light absorption range through localized surface plasmon resonance (LSPR) excitation.[26,61] Moreover, the plasmonic effect in metal-semiconductor heterostructures forming a Schottky junction allows the delocalisation of electrons and holes.[26,62] This junction enables the photogenerated electron to move in a specific direction depending on the type of the semiconductor.[22] In n-type semiconductors, the electrons will be transferred to the metal, whereas in p-type semiconductors, electrons will be transferred to the semiconductor.[63] The overall plasmonic effect can significantly enhance PC performance. For instance, TiO_2 with attached Au NPs exhibits a 66 times higher PC activity in water-splitting due to the increase of the electron-hole generation rate.[64]

When designing a multi-component photocatalyst, both the surface and the interface facets need to be controlled.[44] Approaches already mentioned above for mono-component semiconductors can also achieve surface facet control in multi-component photocatalysts. On the other hand, the interface design using different components can help accumulate charge carriers and increase their transfer efficiency. The key factors that must be considered for an efficient charge carrier separation on heterointerfaces, and thus for an efficient PC activity are 1) the facet-dependent ability to accept electrons or holes, considering the accumulation of charge carriers on specific facets, 2) the facet-dependent electronic band structure, which influences the interfacial charge transfer, and 3) the interfacial structural and electronic couplings relying on the facet contacts, wherein semiconductor-metal structures the plasmonic effect plays an

important role.[42] Therefore, potential advantages of multi-component heterostructures require an understanding of how to control their surfaces and interfaces.

A common approach for creating multi-component photocatalysts is the self-assembly of two or more independent components[65,66] or the growth of one component on already existing surface facets of the other component.[67] The latter case can be combined with the aforementioned thermodynamic and kinetic approaches to tailor crystals in mono-component systems. For instance, when tailoring PdPt nanocrystals' facets with different capping agents, two PdPt/TiO$_2$ interfaces formed by different facets were observed in the literature.[68] Overall, capping agents are widely used for achieving interface facet control for synthesising multi-component photocatalysts in solution-based processes.

However, other strategies must be developed to progress in this research field. Currently, potential drawbacks of solution-based processes include long processing times, expensive precursors,[69] and the already addressed effects of capping agents on the PC performance.[42,53,55] Capping agent-free facet-controlled synthetic approaches include other solution-based approaches, such as electrodeposition techniques[70] and hydrothermal routes,[71] and gas-phase syntheses.[72,73] In this work, gas-phase processes are of particular interest, aiming to evaluate the PC performance in the absence of capping agents subsequent to this study.

As already discussed above, several intermediate-size bandgap semiconductors have proven their suitability in PC applications by controlling their surface and combining them with other materials. Some common semiconductors for PC water-splitting are CdS,[22,33,34,74] g-C$_3$N$_4$,[22,33,35] and most importantly TiO$_2$,[22,25,27,29,30] whereas noble metals such as Pt[68,75] or Au[34,64] are widely used as co-catalysts to achieve high PC activity. However, the disadvantages of noble metal co-catalysts are their high cost, low abundance, and sensitivity to poisoning,[76] which decreases their activity, highlighting the necessity to find efficient, earth-abundant, low-cost photocatalysts.

Transition metal phosphide (TMP) semiconductors are promising candidates for facilitating efficient H$_2$ production due to their abundance, stability, and versatility. They can work in photocatalysis and photoelectrocatalysis as mono-component catalysts or in combination with co-catalysts.[38,77,78] The multi-electron orbitals of P are likely to lead to better chemical properties of TMPs compared to nitrides.[36] The strong M-P bond in the crystal results in high corrosion resistance in acidic mediums and high thermal and structural stability.[79,80] While

metal-richer phosphides, like MP or M$_2$P, show metallic behaviour with electric and thermal conductivity similar to noble metals,[81] P-richer TMPs have semiconductor properties,[79,82] where the electronegativity of P restricts the electron delocalisation in the metal.[83] In addition, experimental data show that the best performances in HER correspond to the TMPs with higher P content.[46,84–86] The electronegativity of P results in drawing electrons from the metal, acting as a negatively-charged proton trap during the redox reaction.[87] P also has a significant effect on H$_2$ desorption. The presence of P dilutes the density of the metal on the surface, which decreases the binding energy with H$_2$, favouring its desorption.[43,46]

TMPs synthesis strategies can be classified into solution-phase and gas-solid reactions.[36,73,88,89] For the first approach, TMPs are usually synthesised using organic P sources, like triphenylphosphine and tri-n-octylphosphine. Control over the particles' size, morphology, and stoichiometry can be achieved by adjusting the reaction parameters, such as the temperature or precursor ratios.[73] On the other hand, gas-solid reactions usually involve hypophosphites, which can decompose and produce phosphine (PH$_3$). This approach requires working in an air-free environment and implies working with toxic and pyrophoric P-containing substances.[73] Additionally, white and red P can also be used to prepare mono- and multi-component TMPs. However, rigorous control of the reaction is required due to the formation of white P and/or PH$_3$.[88,89]

P can react with a wide range of elements to form phosphides. The most common TMPs in photocatalysis are based on Fe,[36,38,43] Co,[36,38,43,86] Mo,[36,43,46] Ni,[36,38,43,74,84,85,90–92] and Cu.[27,36,43,72,77,93,94] Ni and Cu are earth-abundant metals and their phosphides have promising PC properties. According to the literature,[43,85] the main Ni phosphides used for PC water-splitting are Ni$_2$P, an n-type semiconductor with a calculated indirect bandgap energy of 1.31 eV,[92] Ni$_{12}$P$_5$, an n-type semiconductor with a calculated bandgap energy of 0.88 eV,[74] and especially Ni$_5$P$_4$, which exhibits the best HER activity among the three phases.[43,84,85] On the other hand, Cu$_3$P is a p-type semiconductor due to a high density of Cu vacancies,[95] with a direct bandgap energy of 1.3–1.6 eV.[27,96] Cu$_3$P is usually combined with n-type semiconductors[97] or metals[93] to enhance the PC performance. Its promising electronic structure and mechanical and thermal stability make Cu$_3$P an ideal candidate for water-splitting.[94] The controlled combination of Cu- and Ni-based TMPs could result in an efficient, non-noble metal-containing, and sustainable photocatalyst.

This study aims to examine the synthesis of Ni and Cu phosphides by gas-solid reactions and form different phases with specific interfaces by varying the synthesis parameters. Data for this study were collected using an environmental transmission electron microscope (TEM) equipped with a gas handling system capable of supplying PH_3. The findings of this project intend to provide an elemental understanding of the Ni-Cu-P system, allowing the design of advanced NP heterostructures with potential applications in PC water-splitting.

2   Materials and Methods

2.1   Experiments

- **Ni-Cu NP synthesis and deposition:** The bimetallic NPs were generated in a home-built spark ablation system using Cu as the anode and Ni as the cathode. An N_2/H_2 gas mixture carried the generated agglomerates through a furnace kept at 900 ℃ for sintering. Subsequently, a differential mobility analyser (DMA) selected particles with a particular mobility diameter. NPs with a diameter of approximately 30 nm were deposited on microelectromechanical systems (MEMS)-based heating chips *via* the electrostatic precipitator.[72,98]

- **Annealing:** For the first experiment, the bimetallic particles were annealed at 650 ℃ for 12 min, with the supply of 2.0 sccm H_2, to remove oxides and contamination from the NP surfaces. For the second experiment, two annealings at 650 °C were performed without any H_2 supply – the first for 12 min and the second for 10 min.

- **Phosphides synthesis:** The TMP synthesis was performed by the controlled supply of PH_3 *via* the side port injector integrated into the column and connected to the gas handling system. Different PH_3 flows were supplied directly to the heated area of the MEMS-based chip. For experiment 1, the Ni-Cu particles were kept at 350 ℃ after the annealing with H_2, and 0.2 sccm of PH_3 were added. The phase transformation occurred a few seconds after PH_3 was supplied. For experiment 2, the Ni-Cu particles were annealed without H_2 at 650 ℃, and approximately after 8 min, 0.4 sccm of PH_3 were added. Detailed graphs representing the process parameters used for both experiments are shown in Figures A and B.

- **Environmental TEM imaging and characterisation:** Experiments were performed with a Hitachi HF-3300S environmental TEM operated at 300 kV. The microscope can record high-resolution TEM (HRTEM) images/movies with a relatively high temporal resolution using a *GATAN OneView IS camera*. Moreover, it allows performing scanning TEM (STEM) and energy-dispersive X-ray spectroscopy (EDS) analyses.

2.2 Data processing

- **Environmental TEM data processing:** The environmental TEM images and movies were recorded and processed with *DigitalMicrograph* from *Gatan* (Version 3.50.3584.0). The HRTEM movie used for Figure 5 was acquired with a frame rate of 20 frames per second, and the one used for Figure 11 was acquired with a frame rate of 25 frames per second. HRTEM images extracted from both movies were generated by combining 10 averaged consecutive frames. *DigitalMicrograph* was also used to calculate power spectra of specific HRTEM image regions by applying a fast Fourier transform (FFT) on the selected image region. This allowed the analysis of the present phases in the samples.

- **Power spectra analysis:** Power spectra of the NPs were overlaid with simulated electron diffraction patterns using *SingleCrystal* and *CrystalMaker* from *CrystalMaker Software Ltd.* (Version 4.1.6). The *CIF* files were downloaded from the *Inorganic Crystal Structure Database* of the *FIZ Karlsruhe – Leibniz Institute for Information Infrastructure*.

- **EDS and STEM-EDS data processing:** The EDS data were acquired and processed with *AZtec* from *Oxford Instruments Nanotechnology Tools Ltd.* (Version 5.0). The error of the compositional analysis is ~ 0.5 %. However, due to the small size of the NPs, the error is expected to be more significant.

- **Figures:** The figures of this work were prepared using *PowerPoint* from *Microsoft Corporation* (Version 2204) and *GIMP* (Version 2.10.30).

3 Results and Discussions

Ni-Cu NPs were generated in a home-built spark ablation system and deposited on MEMS-based heating chips for in-situ TEM analysis. The diameter of the deposited NPs was approximately 30 nm. As revealed in their binary phase diagram, Ni and Cu show complete miscibility over the whole composition range.[99]

3.1 Experiment 1

STEM-EDS elemental maps of NPs recorded before the phosphorisation (Figure 3) showed an average NP composition of 79 at% $\pm$ 4 at% Ni and 21 at% $\pm$ 4 at% Cu (7 NPs were measured). Both elements were homogeneously distributed within the NPs. The low Cu content in the NPs is due to the fact that fewer Cu atoms were ablated from the corresponding electrode during the NP generation. Contamination on the NP surfaces could be observed exemplarily shown in Figure 3a. The contamination could originate from the oxidation of the metals or the electron beam-induced deposition of carbon from hydrocarbon sources present in the microscope.
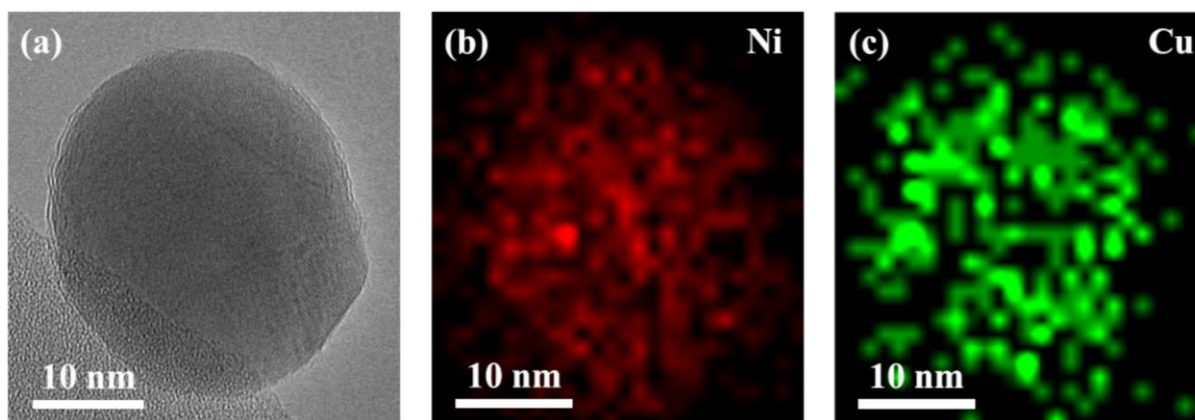

Figure 3. (a) HRTEM image of a Ni-Cu NP acquired at 350 °C without a previously performed H_2 treatment. (b) Ni ($K\alpha_1$) and (c) Cu ($K\alpha_1$) STEM-EDS elemental maps of the NP presented in (a).

Although most NPs had a spherical shape and the desired size (Figure C), some nanostructures showed incomplete compaction. Those structures revealed a sintering neck and similar composition in both NP parts (Figure 4). EDS spectra also showed that before the annealing, a phase that might be a metal arsenide was present, most likely formed at the interface of the two Cu/Ni solid alloy phases. The deposited NPs were annealed at 650 °C with an H_2 supply of 2 sccm to remove surface oxides. The arsenide phase was examined after the annealing and could be assigned to ternary $(Ni, Cu)_5As_2$ phase using the phase's power spectrum (Figure D).
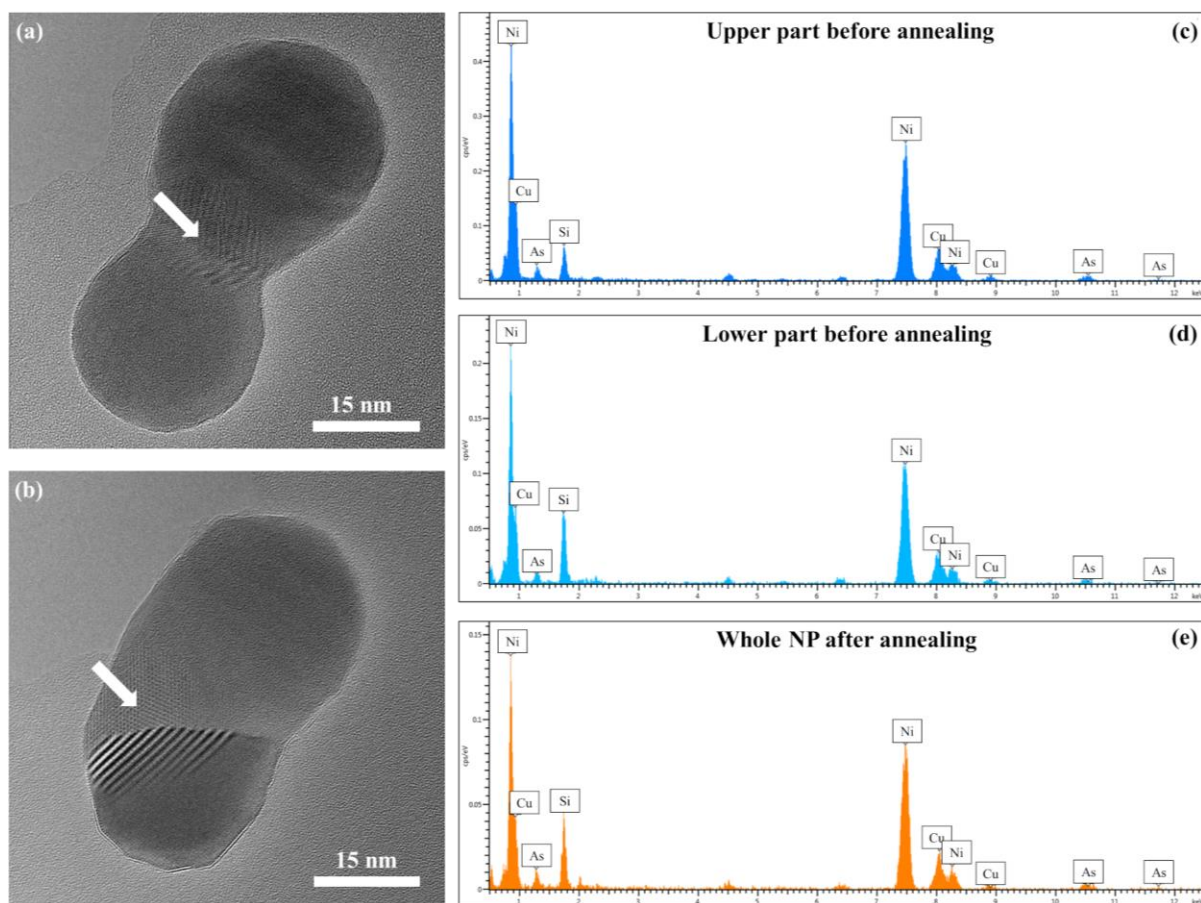
Figure 4. HRTEM images of a Ni-Cu NP acquired at 350 ℃ (a) before and (b) after the annealing performed at 650 ℃ with an H_2 supply of 2.0 sccm. An additional phase was observed at the interface of the two Cu/Ni solid alloy phases. It is expected that the additional phase formed due to the As background pressure in the microscope caused by contamination from previous experiments. EDS spectra of the NP's (c) upper part and (d) lower part before the annealing. (e) EDS spectrum of the NP after the annealing. The Si peaks observed in the EDS spectra correspond to the chip's SiN_x membrane on which the NPs were deposited.

After the H_2 treatment at 650 °C, 0.2 sccm PH_3 were supplied to the sample kept at 350 ℃. A graph showing the used process conditions of experiment 1 is presented in Figure A. The dynamic processes occurring as part of the phase transformation are shown as a sequence of HRTEM images extracted from an HRTEM movie (Figure 5). Before adding PH_3, the NP composition was homogeneous, and its morphology was spherical (Figure 5a). The metals' chemical reaction with PH_3 yielded a faceted nanostructure growing on the upper-right part of the NP indicated by a white arrow (Figure 5b-c). The phosphide phase, which could be assigned to Ni_5P_4 oriented in its [0001] zone axis (Figure 5e), kept growing, as revealed and indicated by a white arrow in Figure 5d. Finally, after approximately 51 s of PH_3 supply, the NP stopped growing, resulting in the nanostructure presented in Figure 5f. It is worth mentioning that no Cu-phase could be identified in this NP. There are two possible explanations. One likely

scenario is that the total Cu amount in the NP was small enough to be completely dissolved in the Ni_5P_4 phase. However, the lattice parameters correlated to the reflections in the power spectrum did not show alterations compared to the pure Ni_5P_4 phase represented by the simulated electron diffraction pattern in Figure 5e. On the other hand, similar Ni and Cu radii[59] would lead to negligible expansion or contraction of the phase, resulting in a similar pattern. The other possibility is that a Cu-based phase was attached to the Ni_5P_4 phase but oriented off a specific zone axis, making its observation difficult. Since no EDS data of this NP were acquired, a detailed characterisation of the present phase(s) was not possible.
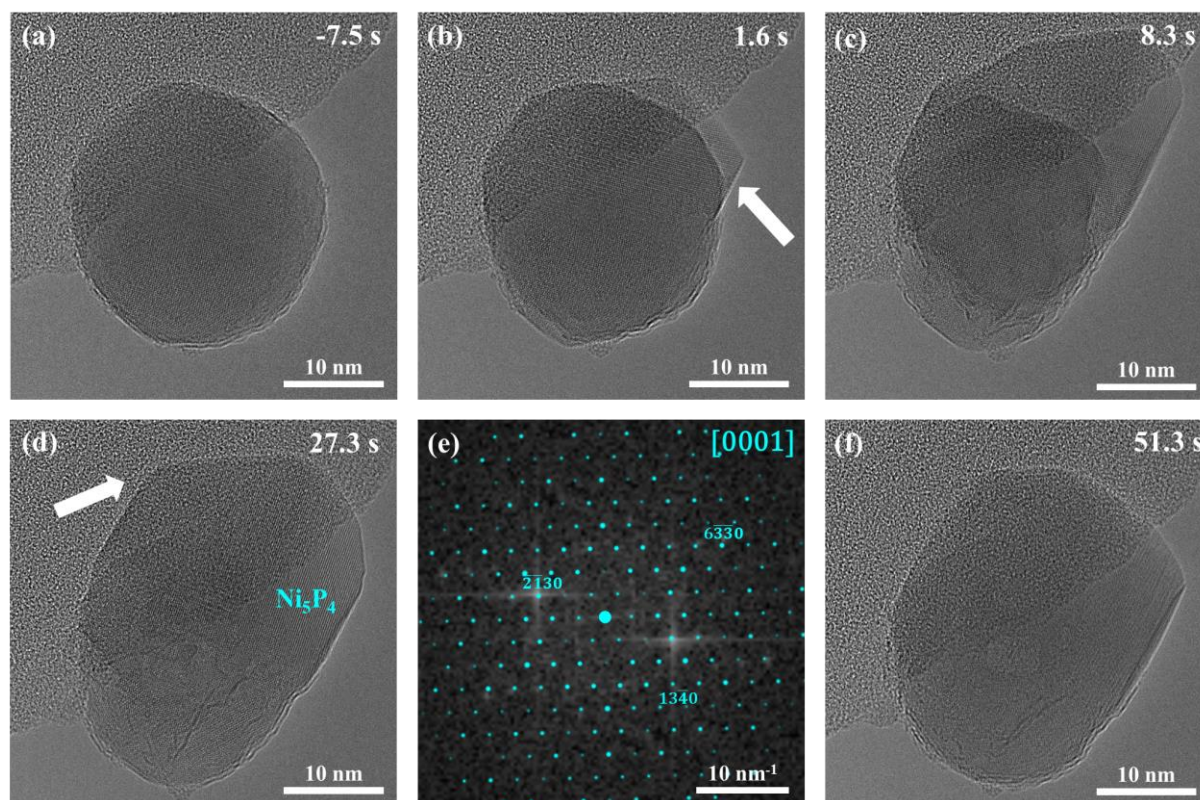

Figure 5. Selected averaged frames of an HRTEM movie at (a) -7.5 s, (b) 1.6 s, (c) 8.3 s, (d) 27.3 s, and (f) 51.3 s after supplying 0.2 sccm PH_3 to a Ni−Cu NP kept at 350 °C. (e) The power spectrum corresponding to (d) was overlaid with a matching simulated electron diffraction pattern of the Ni_5P_4 phase[100] oriented in its [0001] zone axis.

A detailed characterisation of a NP just after starting the PH_3 supply revealed the presence of two different phases (Figure 6). The power spectrum of the HRTEM image in Figure 6b shows the presence of a relatively large Ni_5P_4 phase and a minor Cu_3P phase. STEM-EDS elemental maps of the NP in Figure 6a confirmed the assigned identity of the phases (Figure 6c-e). Moreover, EDS data confirmed that no significant As content was present in the NP.
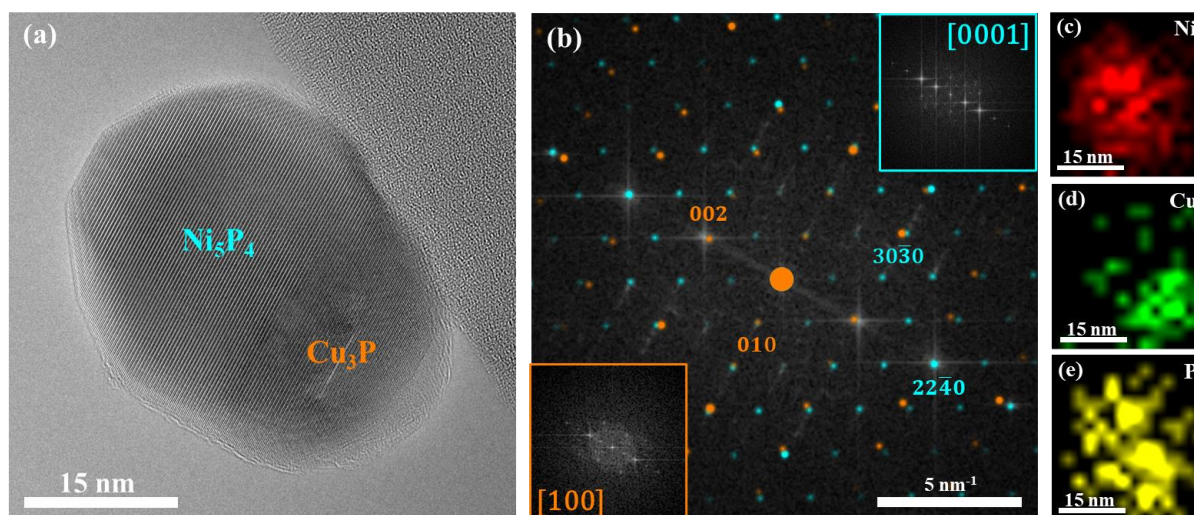
Figure 6. (a) HRTEM image of a Ni-Cu NP acquired at 350 ℃ just after starting the PH$_3$ supply. (b) Power spectra of (a) with overlaid simulated electron diffraction patterns of the Ni$_5$P$_4$ ([0001] zone axis, blue pattern) and Cu$_3$P ([100] zone axis, orange pattern[101] phases are shown. The phases' locations are indicated with labels in (a). STEM-EDS elemental maps of (d) Ni (Kα_1), (e) Cu (Kα_1), and (f) P (Kα_1) confirm the presence of the addressed phases in the NP revealed in (a).

Subsequently, temperature annealings under different conditions were performed (see Figure A). The resulting NPs, where one is exemplarily shown in Figure 7, revealed similar results as the NP in Figure 6. The overlay of the power spectra corresponding to the HRTEM image in Figure 7a with matching simulated electron diffraction patterns allows the association of Ni$_5$P$_4$ to the larger phase (Figure 7b) and Cu$_3$P to the smaller one (Figure 7c). The power spectra analysis revealed that the sharp interface between the two phases was formed by Ni$_5$P$_4\{1\bar{2}10\}$ and Cu$_3$P$\{001\}$ facets.

STEM-EDS maps confirmed the chemical compositions associated with the attributed phases in the NP (Figure 7d-g). A small amount of As was likely present in the bottom right part of the NP, as suggested by the corresponding EDS map (Figure 7g). The data indicate that As was not exchanged completely with P after supplying PH$_3$. The chemical composition of the Ni-based phase could be determined to be approximately 54 at% Ni, 42 at% P, and 4 at% Cu. On the other hand, a chemical composition of approximately 46 at% Cu, 38 at% P, and 16 at% Ni was observed for the Cu-based phase, indicating the incorporation of Ni atoms in the Cu$_3$P phase. However, it is worth mentioning that the volume of the Cu-based phase was extremely small, making a precise quantification of the chemical composition impossible. Still, the trends are visible and confirm the conclusions from above.
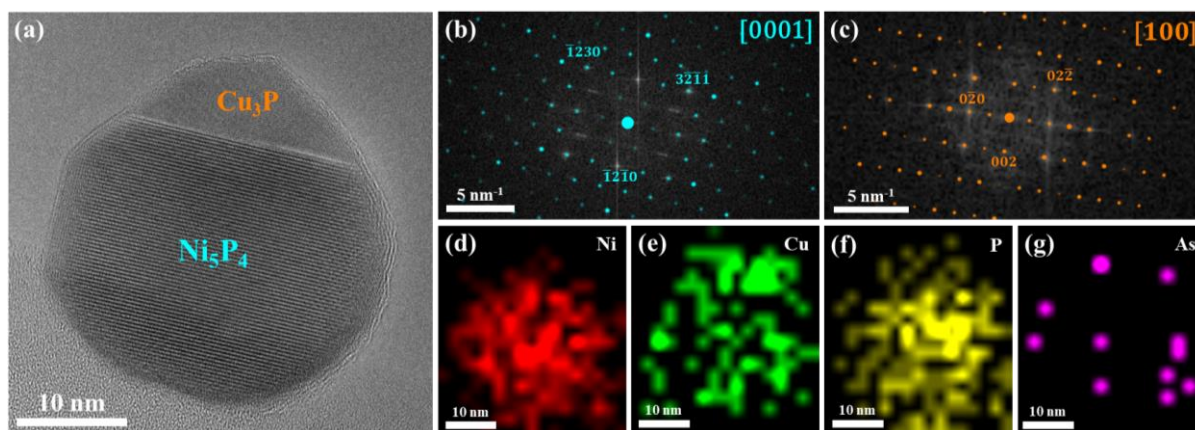
Figure 7. (a) HRTEM image of a Ni-Cu NP acquired at 400 °C after stopping the PH$_3$ supply. Power spectra of the (b) Ni-based and (c) Cu-based NP phases are shown. Simulated electron diffraction patterns of (b) the Ni$_5$P$_4$ phase-oriented in the [0001] zone axis and (c) the Cu$_3$P phase oriented in the [100] zone axis matched the power spectra confirming their presence. The phases' locations are indicated with labels in (a). STEM-EDS elemental maps of (d) Ni (Kα_1), (e) Cu (Kα_1), (f) P (Kα_1), and (g) As (Kα_1) confirm the presence of the addressed phases in the NP revealed in (a).

Finally, the temperature was increased step-wise after stopping the PH$_3$ supply (see Figure A). The effect of the temperature on the NPs was evaluated, emphasizing potential dynamic processes initiated by the energy input. The studied NP had a spherical shape at 228 s after increasing the temperature to 550 °C (Figure 8a). The power spectrum of the NP (Figure 8d) allows the identification of the ternary phosphide (Ni, Cu)$_5$P$_4$ phase, oriented in its [0001] zone axis by overlaying it with a matching simulated electron diffraction pattern. Interestingly, at 311 s after increasing the temperature to 550 °C, another phase separated from the (Ni, Cu)$_5$P$_4$ phase on the top part of the NP, as indicated by a white arrow (Figure 8b). The power spectrum of the whole NP revealed new reflections, as indicated by white circles, which suggests the separation of a Cu-based phase (Figure 8e). The primary phase could still be assigned to the Ni$_5$P$_4$ phase in its [0001] zone axis, with the incorporation of Cu atoms expected to be significantly lower. Finally, when the NP was heated to 678 °C and kept at the same temperature for approximately 1 min, the separated phase rearranged at the surface of the Ni$_5$P$_4$ phase (Figure 8c).

We concluded that the Ni$_5$P$_4$ phase initially contained significant amounts of Cu atoms based on those observations. The Ni$_5$P$_4$ phase formed a sharp interface with the Cu-based phase involving a Ni$_5$P$_4$\{3$\bar{2}\bar{1}$0\} facet. Unfortunately, the Cu-based phase was not oriented in one of its zone axes, making a more detailed characterization impossible. The Cu-based phase was likely to be Cu$_3$P due to Cu$_3$P\{100\} planes that could be associated with the intense reflections

highlighted by the white circles in Figure 8f. However, EDS data were required to determine the presence of the Cu_3P phase during this process stage.
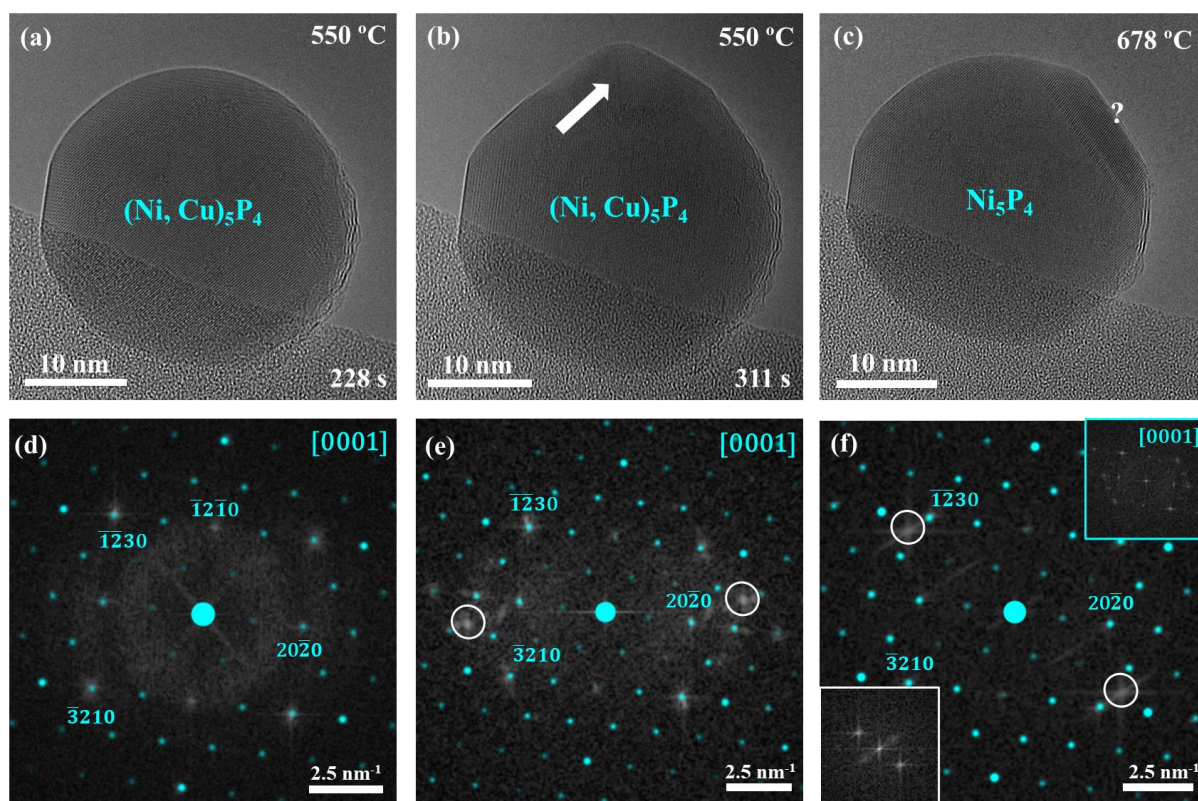

Figure 8. HRTEM images of the same Ni-Cu NP acquired at (a) 550 °C, (b) at the same temperature and a longer annealing time, and (c) at 678 °C. HRTEM images were acquired after (a) 228 and (b) 311 s of annealing at 550 °C. (c) The HRTEM image was acquired after 52 s of annealing at 678 °C. (d-f) Power spectra of the NPs shown in (a-c) with overlaid simulated electron diffraction patterns of the (Ni, Cu)$_5$P$_4$ ([0001] zone axis, blue pattern) phase. The power spectra of the Ni$_5$P$_4$ (blue frame) and the separated phase (white square) are included as insets in (f).

Subsequently, the sample was heated to 700 °C, which caused the rearrangement of the Cu-based phase located in the left part of the NP, as indicated with a white arrow in Figure 9a. The temperature was decreased to 400 °C to achieve better imaging of the particle (Figure 9b). The power spectrum of the HRTEM image in Figure 9b confirms that the larger phase was Ni$_5$P$_4$ and that the smaller phase was Cu_3P (Figure 9c). Moreover, the sharp interface between the two phases was identified as a Ni$_5$P$_4\{10\bar{1}0\}$/$Cu_3P\{010\}$ interface. These results suggest that, as already mentioned above, the separated phase in Figure 8c was very likely Cu-based and the energy input, either from the temperature or the electron beam, caused the rearrangement of the phases.
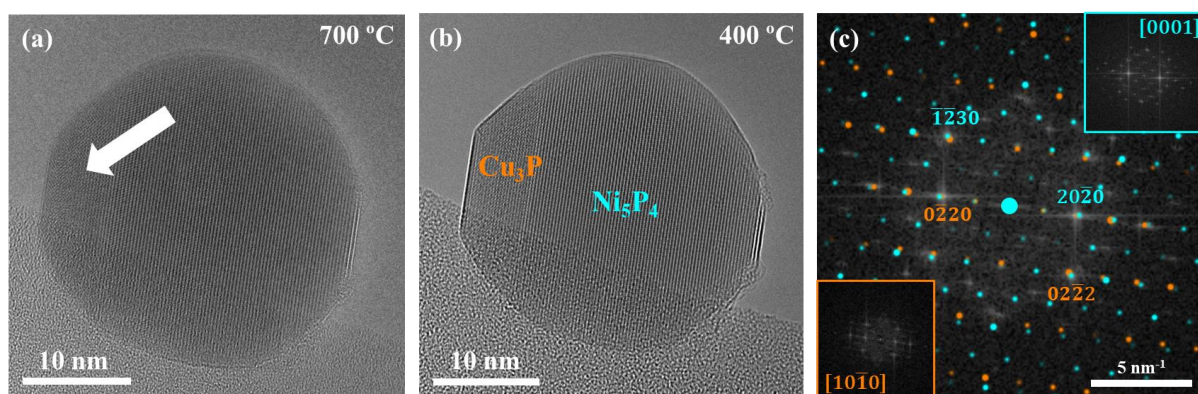
Figure 9. HRTEM images of the same Ni-Cu NP acquired at (a) 700 °C and (b) 400 °C. (c) Power spectrum of the NP shown in (b) with overlaid simulated electron diffraction patterns of the Ni_5P_4 ([0001] zone axis, blue pattern) and Cu_3P ([100] zone axis, orange pattern) phases. The power spectra of the pure phases are shown as insets in (c). Labels in (b) indicate the phases' locations.

3.2 Experiment 2

In the second experiment, the NPs also revealed As contamination before supplying PH_3, as demonstrated by STEM-EDS elemental maps acquired at 350 °C (Figure E). Moreover, a small amount of P was found in the NP before any PH_3 was supplied (71 at% Ni, 22 at% Cu, 5 at% As, and 2 at% P). After 8 min of annealing at 650 °C without adding H_2, another NP showed different phases (Figure 10a) instead of a homogeneous spherical NP as in Figure 3. Due to their complete miscibility over the whole composition range already addressed above,[99] Ni and Cu formed a $Ni_{1-x}Cu_x$ solid solution. The power spectrum of the NP was overlaid with simulated electron diffraction patterns of the $Ni_{1-x}Cu_x$ phase for the [110] and [101] zone axes (Figure 10b). Therefore, the NP revealed a twinned $Ni_{1-x}Cu_x$ phase with an interface formed by {111} facets. The formation of interfaces involving {111} facets is common for cubic systems, as reported in the literature.[102] The two phases had approximately the same composition, as observed in STEM-EDS elemental maps (Figure 10c-e).

Moreover, As contamination was also observed in the right part of the NP. As reacted with the $Ni_{1-x}Cu_x$ phase, forming an arsenide. The arsenide could be assigned to Ni_5As_2, but as Cu was also part of the phase, it is expected that Cu was also incorporated into the Ni_5As_2 phase, forming a ternary Ni-Cu arsenide phase (($Ni, Cu)_5As_2$) with a composition in accordance with the Ni:Cu ratio of the initial metal NP. EDS data of the As-rich phase (Ni 73 at%, Cu 15 at%, and As 12 at%) are in good agreement with this hypothesis. It is worth mentioning that it is likely that the NP already presented the twinned phases before the chemical reaction with As occurred.
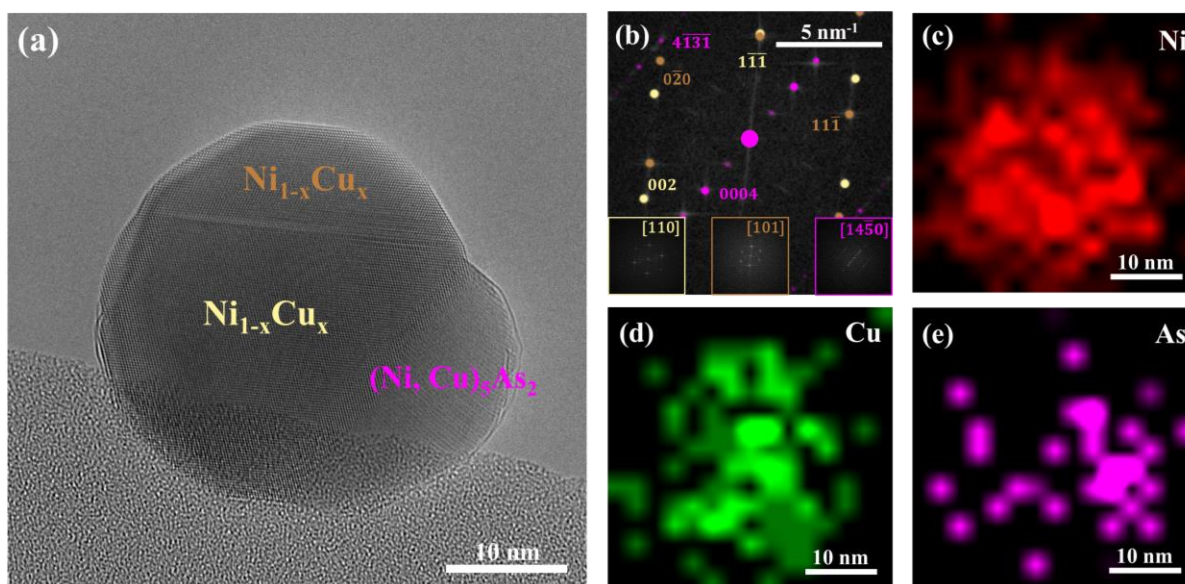
24

Figure 10. (a) HRTEM image of a Ni-Cu NP with As contamination acquired at 650 ℃ without previous H$_2$ treatment and before the PH$_3$ supply. (b) Power spectrum of the whole NP in (a) with overlaid simulated electron diffraction patterns of Ni$_{1-x}$Cu$_x$ oriented in the [110] zone axis (pale yellow pattern)[103,104], Ni$_{1-x}$Cu$_x$ oriented in the [101] zone axis (brown pattern), and (Ni, Cu)$_5$As$_2$ oriented in the [14$\bar{5}$0] zone axis (purple pattern)[105]. The phases' locations are indicated with labels in (a). STEM-EDS elemental maps of (c) Ni (Kα_1), (d) Cu (Kα_1), and (e) As (Kα_1) highlight the chemical distribution in the NP revealed in (a).

The chemical reaction with P was performed at 650 °C by supplying 0.4 sccm of PH$_3$. A graph summarising the process parameters of experiment 2 is shown in Figure B. As PH$_3$ reacted with the NP, its morphology changed, as shown in a sequence of HRTEM images extracted from an HRTEM movie (Figure 11). The sequence reveals the chemical reaction of Ni and Cu with P resulting in the growth of a new phase while consuming the Ni$_{1-x}$Cu$_x$ phases (Figures 11a-c). The initially present (Ni, Cu)$_5$As$_2$ phase acted as a nucleus for the new phase and remained attached to the NP during the transformation process. The power spectra corresponding to the HRTEM images in Figures 11a-c confirm the abovementioned observations (Figure 11d-f). Moreover, the chemical reaction led to the evolution of a single Ni-Cu phosphide phase from the twinned Ni$_{1-x}$Cu$_x$ phase, which implies that Cu was incorporated in the Ni-rich phosphide phase.
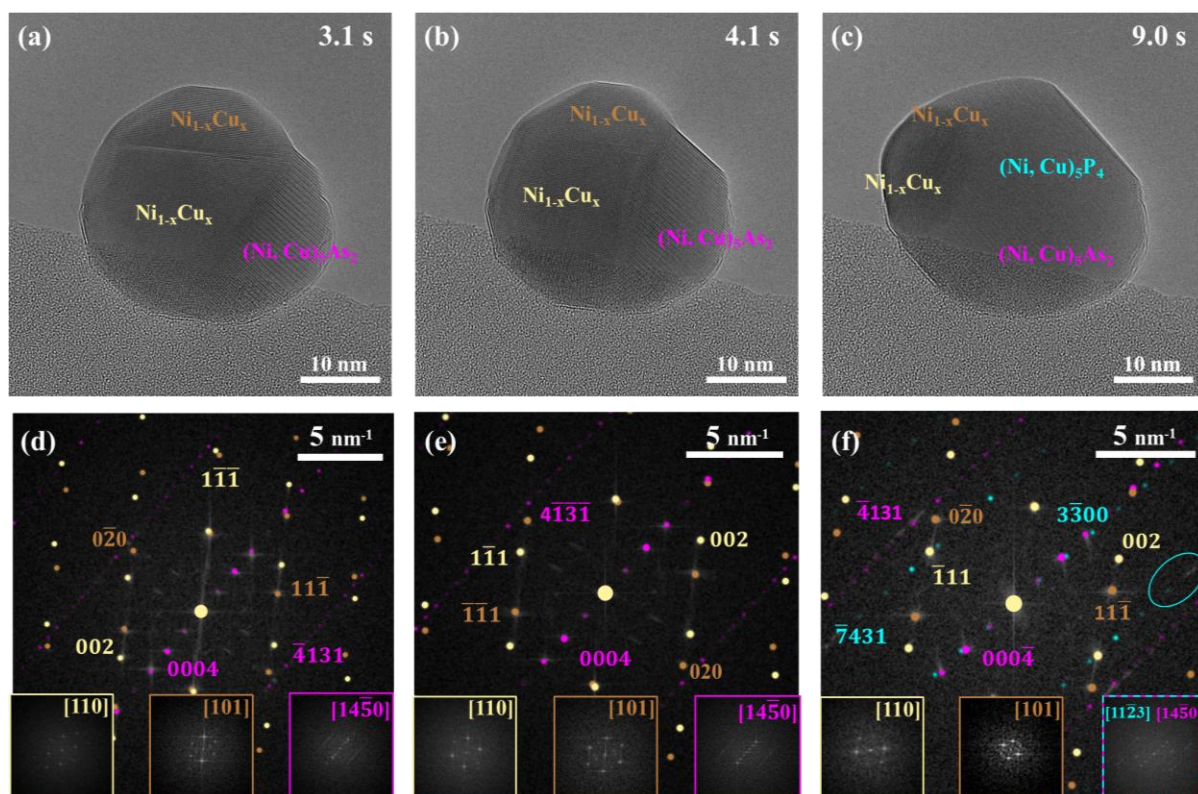
Figure 11. Selected averaged frames of an HRTEM movie at (a) 3.1 s, (b) 4.1 s, and (c) 9.0 s after supplying 0.4 sccm PH_3 to the same NP as in Figure 10a kept at 650 °C. (c) The $(Ni, Cu)_5P_4$ phase nucleated at the $(Ni, Cu)_5As_2$ phase and grew by consuming the Ni-Cu solid solution. (d-f) The identity of the present phases was assigned by overlaying the power spectra corresponding to the HRTEM images in (a-c) with matching simulated electron diffraction patterns of $Ni_{1-x}Cu_x$ oriented in the [110] zone axis (pale yellow pattern), $Ni_{1-x}Cu_x$ oriented in the [101] zone axis (brown pattern), $(Ni, Cu)_5As_2$ ([$14\bar{5}0$] zone axis, purple pattern), and $(Ni, Cu)_5P_4$ ([$11\bar{2}3$] zone axis, blue pattern) phases. Labels in (a-c) indicate the phases' locations. In contrast to (d) and (e), new reflections can be observed (marked with a blue ellipse) in (f), corresponding to the formed $(Ni, Cu)_5P_4$ phase. It should be noted that in the bottom left inset of (f), the power spectrum includes both the $(Ni, Cu)_5As_2$ and $(Ni, Cu)_5P_4$ phases.

Finally, the $Ni_{1-x}Cu_x$ phases were completely consumed, resulting in a ternary phosphide (Figure 12a). Interestingly, phase separation was observed when the temperature was decreased from 650 °C to 350 °C without stopping the PH_3 supply (Figure 12b). The new phase could be identified as CuP_2 *via* the overlay of the power spectrum with a simulated electron diffraction pattern of this phase (Figure 12c). The Ni-based phase could still be assigned to Ni_5P_4 (Figure 12c). The EDS analyses of the phases' chemical composition confirmed the allocation of the Ni_5P_4 phase (58 at% Ni, 39 at%, and 3 at% Cu), but showed a mismatch for the Cu-based phase (42 at% Cu, 45 at% P, and 13 at% Ni). The mismatch might be caused by the small volume of the Cu-based phase and the resulting significant error in the EDS measurements. Therefore, the Cu phase could be either assigned to the CuP_2 phase (33 at% Cu) or the Cu_3P phase (75 at% Cu). However, the pattern of the power spectrum and the relatively high PH_3 flow used for this

experiment suggest the presence of a P-richer phase. Moreover, STEM-EDS elemental maps (Figure 12d-f) revealed that after the PH$_3$ supply, P entirely replaced As in the NP, as the latter was not detected in the maps. Finally, it is also worth mentioning that the energy input of the electron beam could affect the processes discussed above.[72]
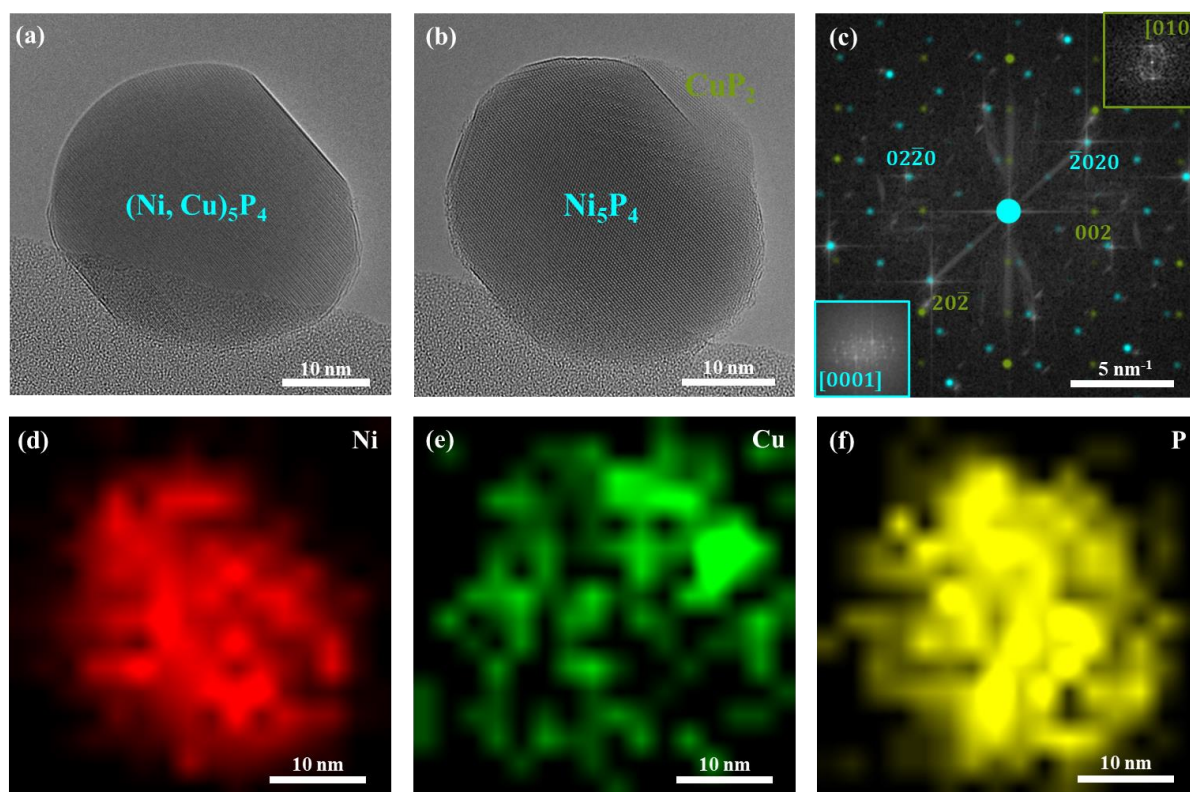

Figure 12. (a) HRTEM image of the same NP as presented in Figure 10 and kept at 650 °C after the chemical reaction was completed. (b) The HRTEM image reveals the NP after decreasing the temperature to 350 ºC. The PH$_3$ supply remained unaltered. The temperature decrease led to separating the ternary phosphide into the Ni$_5$P$_4$ and CuP$_2$ phases. (c) The power spectrum of the NP in (b) with overlaid simulated electron diffraction patterns of the Ni$_5$P$_4$ ([0001] zone axis, blue pattern) and CuP$_2$ ([010] zone axis, green pattern)[106] phases allowed the allocation of the phases suggested above. (d) STEM-EDS elemental maps of Ni (Kα_1), (e) Cu (Kα_1), and (f) P (Kα_1) confirm the phase separation process observed in the NP in (b).

4   Conclusions

The deposited NPs revealed a composition of approximately 80 at% Ni and 20 at% Cu. The metals formed a $Ni_{1-x}Cu_x$ solid solution, which in some cases were twinned. During the conduction of the experiments, As contamination had an unintentional impact on the NPs, forming ternary arsenides. However, by supplying PH_3 at high temperatures, P could partly and, in some cases, completely replace the As from the NPs.

When Ni-Cu NPs reacted with relatively low flows of PH_3, the formation of single-phase $(Ni, Cu)_5P_4$ and two-phase Ni_5P_4-Cu_3P NPs was observed. We conclude that a limited amount of Cu can be dissolved in the Ni_5P_4 phase. Therefore, the initial bimetallic NPs' Ni:Cu atomic ratio is elemental to control the formation of different phases. We expect that a higher Cu content in the NPs will likely lead to two-phase NPs consisting of Cu- and Ni-based phosphides. Moreover, the impact of temperature annealing on the arrangement of the phases has been observed. Consequently, temperature annealings show potential in rearranging heterointerfaces and changing the involved facets. In some cases, the characterisation of the NPs revealed defined Ni_5P_4/Cu_3P interfaces with specific facets involved in the formation.

When the metallic NPs reacted with higher PH_3 flows at higher temperatures, the ternary $(Ni, Cu)_5P_4$ phase formation was observed. We conclude that the elevated temperatures led to a higher solubility of Cu atoms in the Ni phosphide phase. Moreover, when the temperature was decreased, a Cu-based phase separated from the $(Ni, Cu)_5P_4$ phase, lowering its Cu content. The separated Cu-based phase could be assigned to the CuP_2 phase.

Overall, these results indicate that different phases can be formed by adjusting different parameters, including the initial atomic ratio, precursor flow, and temperature. Furthermore, the experiments proved that the NPs are stable up to 700 °C, as heat treatment did not affect the final formation of the Ni_5P_4, Cu_3P, and CuP_2 phases. According to the literature, the Ni_5P_4 and Cu_3P phases exhibit favourable activity for water-splitting.[74,94] Therefore, combining those two phases formed by earth-abundant elements in a gas-phase process not involving capping agents could significantly improve the PC performance, which will be evaluated in future experiments.

5 Outlook

In this thesis, we have studied the Ni-Cu system with an approximate composition of Ni 80 at% and Cu 20 at%. The atomic ratio of the metals has been presumed as an essential factor in observing specific phases in the ternary Ni-Cu-P nano-system. Therefore, further experiments with different Ni:Cu atomic ratios of the deposited bimetallic NPs could be performed to obtain additional control over the formation of the phases. For that purpose, the NP generation *via* the spark ablation system needs to be optimised for a reproducible deposition of Ni-Cu NPs with specific Ni:Cu atomic ratios. Moreover, further experiments with different PH_3 flows and annealing temperatures could be performed to better understand the processes involved in the reaction of Ni-Cu NPs with PH_3.

A more detailed analysis of surface and interface facet design could be achieved by performing more experiments. Moreover, two different Cu phosphides phases and one Ni phosphide phase were synthesised. However, by altering the synthetic parameters, other phases could be obtained and studied, resulting in a broader knowledge of the Ni-Cu-P nano-system and a better understanding of the nanostructures' interfaces. Future studies will also correlate this system's designed interfaces and phases with the PC performance in water-splitting. One future goal would be to synthesise $Cu-Ni_5P_4$ NPs to achieve better charge carrier separation *via* the plasmonic effect originating in the metallic Cu phase.

Finally, another objective of this work could be the growth of GaP nanowires using Ni-Cu seed particles with the ultimate goal to crystalise the relevant phosphides at the tip of the GaP nanowires after growth. This approach would allow the combination of three different phosphide phases, all showing activity in PC reactions.

6 References

(1)   *2030 Climate Target Plan*. https://ec.europa.eu/clima/eu-action/european-green-deal/2030-climate-target-plan_en (accessed 2022-04-04).

(2)   *Hydrogen Strategy Enabling a Low-Carbon Economy | Department of Energy*. https://www.energy.gov/fecm/downloads/hydrogen-strategy-enabling-low-carbon-economy (accessed 2022-03-22).

(3)   Maeda, K. Photocatalytic Water Splitting Using Semiconductor Particles: History and Recent Developments. *Journal of Photochemistry and Photobiology C: Photochemistry Reviews* **2011**, *12* (4), 237–268.

(4)   Ifkovits, Z. P.; Evans, J. M.; Meier, M. C.; Papadantonakis, K. M.; Lewis, N. S. Decoupled Electrochemical Water-Splitting Systems: A Review and Perspective. *Energy & Environmental Science* **2021**, *14* (9), 4740–4759.

(5)   Ran, J.; Zhang, J.; Yu, J.; Jaroniec, M.; Qiao, S. Z. Earth-Abundant Cocatalysts for Semiconductor-Based Photocatalytic Water Splitting. *Chemical Society Reviews* **2014**, *43* (22), 7787–7812.

(6)   Hisatomi, T.; Domen, K. Progress in the Demonstration and Understanding of Water Splitting Using Particulate Photocatalysts. *Current Opinion in Electrochemistry* **2017**, *2* (1), 148–154.

(7)   Dawood, F.; Anda, M.; Shafiullah, G. M. Hydrogen Production for Energy: An Overview. *International Journal of Hydrogen Energy* **2020**, *45* (7), 3847–3869.

(8)   Song, H.; Luo, S.; Huang, H.; Deng, B.; Ye, J. Solar-Driven Hydrogen Production: Recent Advances, Challenges, and Future Perspectives. *ACS Energy Letters* **2022**, *7* (3), 1043–1065.

(9)   Ni, M.; Leung, M. K. H.; Leung, D. Y. C.; Sumathy, K. A Review and Recent Developments in Photocatalytic Water-Splitting Using TiO2 for Hydrogen Production. *Renewable and Sustainable Energy Reviews* **2007**, *11* (3) 401–425.

(10) Hernández-Ramírez, A.; Medina-Ramírez, I. *Photocatalytic Semiconductors: Synthesis, Characterization, and Environmental Applications*; Springer International Publishing, 2015.

(11) Fujishima, A.; Honda, K. Electrochemical Photolysis of Water at a Semiconductor Electrode. *Nature* **1972**, *238* (5358), 37–38.

(12) Rahman, A.; Khan, M. M. Chalcogenides as Photocatalysts. *New Journal of Chemistry* **2021**, *45* (42), 19622–19635.

(13) Peleyeju, M. G.; Viljoen, E. L. WO3-Based Catalysts for Photocatalytic and Photoelectrocatalytic Removal of Organic Pollutants from Water – A Review. *Journal of Water Process Engineering* **2021**, *40*, 101930.

(14) Mishra, M.; Chun, D. M. α-Fe2O3 as a Photocatalytic Material: A Review. *Applied Catalysis A: General* **2015**, *498*, 126–141.

(15) Ojha, N.; Kumar, S. Tri-Phase Photocatalysis for CO2 Reduction and N2 Fixation with Efficient Electron Transfer on a Hydrophilic Surface of Transition-Metal-Doped MIL-88A (Fe). *Applied Catalysis B: Environmental* **2021**, *292*, 120166.

(16) Yu, J.; Low, J.; Xiao, W.; Zhou, P.; Jaroniec, M. Enhanced Photocatalytic CO2-Reduction Activity of Anatase TiO2 by Coexposed {001} and {101} Facets. *J Am Chem Soc* **2014**, *136* (25), 8839–8842.

(17) Guan, R.; Wang, D.; Zhang, Y.; Liu, C.; Xu, W.; Wang, J.; Zhao, Z.; Feng, M.; Shang, Q.; Sun, Z. Enhanced Photocatalytic N2 Fixation via Defective and Fluoride Modified TiO2 Surface. *Applied Catalysis B: Environmental* **2021**, *282*, 119580.

(18) Yu, J.; Ren, X.; Lu, J.; Bai, H.; Wang, X.; Hu, J.; Huang, H. Cobalt Doping of Porous Graphitic Carbon Nitride with CoN Bonds Promotes Electrocatalytic N2 Fixation under Ambient Conditions. *Journal of Alloys and Compounds* **2022**, *902*, 163862.

(19) Goktas, S.; Goktas, A. A Comparative Study on Recent Progress in Efficient ZnO Based Nanocomposite and Heterojunction Photocatalysts: A Review. *Journal of Alloys and Compounds* **2021**, *863*, 158734.

(20) Keerthana, S. P.; Yuvakkumar, R.; Ravi, G.; Kumar, P.; Elshikh, M. S.; Alkhamis, H. H.; Alrefaei, A. F.; Velauthapillai, D. A Strategy to Enhance the Photocatalytic Efficiency of α-Fe2O3. *Chemosphere* **2021**, *270*, 129498.

(21) Murillo-Sierra, J. C.; Hernández-Ramírez, A.; Hinojosa-Reyes, L.; Guzmán-Mar, J. L. A Review on the Development of Visible Light-Responsive WO3-Based Photocatalysts for Environmental Applications. *Chemical Engineering Journal Advances* **2021**, *5*, 100070.

(22) Fajrina, N.; Tahir, M. A Critical Review in Strategies to Improve Photocatalytic Water Splitting towards Hydrogen Production. *International Journal of Hydrogen Energy* **2019**, *44* (2), 540–577.

(23) Chen, L.; Yang, S.; Zhang, Q.; Zhu, J.; Zhao, P. Rational Design of {0 0 1}-Faceted TiO2 Nanosheet Arrays/Graphene Foam with Superior Charge Transfer Interfaces for Efficient Photocatalytic Degradation of Toxic Pollutants. *Separation and Purification Technology* **2021**, *265*, 118444.

(24) Katal, R.; Masudy-Panah, S.; Tanhaei, M.; Farahani, M. H. D. A.; Jiangyong, H. A Review on the Synthesis of the Various Types of Anatase TiO2 Facets and Their Applications for Photocatalysis. *Chemical Engineering Journal* **2020**, *384*, 123384.

(25) Eidsvåg, H.; Bentouba, S.; Vajeeston, P.; Yohi, S.; Velauthapillai, D. TiO2 as a Photocatalyst for Water Splitting—An Experimental and Theoretical Review. *Molecules 2021, Vol. 26, Page 1687* **2021**, *26* (6), 1687.

(26) Kumar, A.; Choudhary, P.; Kumar, A.; Camargo, P. H. C.; Krishnan, V.; Kumar, A.; Choudhary, P.; Krishnan, V.; Camargo, C. Recent Advances in Plasmonic Photocatalysis Based on TiO2 and Noble Metal Nanoparticles for Energy Conversion, Environmental Remediation, and Organic Synthesis. *Small* **2022**, *18* (1), 2101638.

(27) Yue, X.; Yi, S.; Wang, R.; Zhang, Z.; Qiu, S. A Novel and Highly Efficient Earth-Abundant Cu3P with TiO2 "P–N" Heterojunction Nanophotocatalyst for Hydrogen Evolution from Water. *Nanoscale* **2016**, *8* (40), 17516–17523.

(28) Zhou, K.; Li, Y. Catalysis Based on Nanocrystals with Well-Defined Facets. *Angewandte Chemie International Edition* **2012**, *51* (3), 602–613.

(29) Xu, H.; Reunchan, P.; Ouyang, S.; Tong, H.; Umezawa, N.; Kako, T.; Ye, J. Anatase TiO2 Single Crystals Exposed with High-Reactive {111} Facets toward Efficient H2 Evolution. *Chemistry of Materials* **2013**, *25* (3), 405–411.

(30) Huang, J. F.; Lei, Y.; Luo, T.; Liu, J. M. Photocatalytic H2 Production from Water by Metal-Free Dye-Sensitized TiO2 Semiconductors: The Role and Development Process of Organic Sensitizers. *ChemSusChem* **2020**, *13* (22), 5863–5895.

(31) Qin, S.; Shui, L.; Osuagwu, B.; Denisov, N.; Tesler, A. B.; Schmuki, P. Facet-Control versus Co-Catalyst-Control in Photocatalytic H2 Evolution from Anatase TiO2 Nanocrystals. *ChemistryOpen* **2022**, *11* (3), e202200010.

(32) Ye, X.; Chen, Y.; Ling, C.; Zhang, J.; Meng, S.; Fu, X.; Wang, X.; Chen, S. Chalcogenide Photocatalysts for Selective Oxidation of Aromatic Alcohols to Aldehydes Using O2 and Visible Light: A Case Study of CdIn2S4, CdS and In2S3. *Chemical Engineering Journal* **2018**, *348*, 966–977.

(33) Ran, Y.; Cui, Y.; Zhang, Y.; Fang, Y.; Zhang, W.; Yu, X.; Lan, H.; An, X. Assembly-Synthesis of Puff Pastry-like g-C3N4/CdS Heterostructure as S-Junctions for Efficient Photocatalytic Water Splitting. *Chemical Engineering Journal* **2022**, *431*, 133348.

(34) Majeed, I.; Nadeem, M. A.; Al-Oufi, M.; Nadeem, M. A.; Waterhouse, G. I. N.; Badshah, A.; Metson, J. B.; Idriss, H. On the Role of Metal Particle Size and Surface Coverage for Photo-Catalytic Hydrogen Production: A Case Study of the Au/CdS System. *Applied Catalysis B: Environmental* **2016**, *182*, 266–276.

(35) Rhimi, B.; Wang, C.; Bahnemann, D. W. Latest Progress in G-C3N4 Based Heterojunctions for Hydrogen Production via Photocatalytic Water Splitting: A Mini Review. *Journal of Physics: Energy* **2020**, *2* (4), 042003.

(36) Sun, M.; Liu, H.; Qu, J.; Li, J. Earth-Rich Transition Metal Phosphide for Energy Conversion and Storage. *Advanced Energy Materials* **2016**, *6* (13).

(37) Kahng, S.; Yoo, H.; Kim, J. H. Recent Advances in Earth-Abundant Photocatalyst Materials for Solar H2 Production. *Advanced Powder Technology* **2020**, *31* (1), 11–28.

(38)   Wang, Y.; Kong, B.; Zhao, D.; Wang, H.; Selomulya, C. Strategies for Developing Transition Metal Phosphides as Heterogeneous Electrocatalysts for Water Splitting. *Nano Today* **2017**, *15*, 26–55.

(39)   Morales-Guio, C. G.; Stern, L. A.; Hu, X. Nanostructured Hydrotreating Catalysts for Electrochemical Hydrogen Evolution. *Chemical Society Reviews* **2014**, *43* (18), 6555–6569.

(40)   Wang, W.; Xu, X.; Zhou, W.; Shao, Z. Recent Progress in Metal-Organic Frameworks for Applications in Electrocatalytic and Photocatalytic Water Splitting. *Advanced Science* **2017**, *4* (4), 1600371.

(41)   Khaselev, O.; Turner, J. A. A Monolithic Photovoltaic-Photoelectrochemical Device for Hydrogen Production via Water Splitting. *Science (1979)* **1998**, *280* (5362), 425–427.

(42)   Bai, S.; Wang, L.; Li, Z.; Xiong, Y. Facet-Engineered Surface and Interface Design of Photocatalytic Materials. *Advanced Science* **2017**, *4* (1).

(43)   Li, Y.; Li, R.; Wang, D.; Xu, H.; Meng, F.; Dong, D.; Jiang, J.; Zhang, J.; An, M.; Yang, P. A Review: Target-Oriented Transition Metal Phosphide Design and Synthesis for Water Splitting. *International Journal of Hydrogen Energy* **2021**, *46* (7), 5131–5149.

(44)   Dong, Y.; Li, K.; Luo, W.; Zhu, C.; Guan, H.; Wang, H.; Wang, L.; Deng, K.; Zhou, H.; Xie, H.; Bai, Y.; Li, Y.; Chen, Q. The Role of Surface Termination in Halide Perovskites for Efficient Photocatalytic Synthesis. *Angewandte Chemie* **2020**, *132* (31), 13031–13037.

(45)   Su, Y.; Li, H.; Ma, H.; Robertson, J.; Nathan, A. Controlling Surface Termination and Facet Orientation in Cu2O Nanoparticles for High Photocatalytic Activity: A Combined Experimental and Density Functional Theory Study. *ACS Applied Materials and Interfaces* **2017**, *9* (9), 8100–8106.

(46)   Xiao, P.; Sk, M. A.; Thia, L.; Ge, X.; Lim, R. J.; Wang, J. Y.; Lim, K. H.; Wang, X. Molybdenum Phosphide as an Efficient Electrocatalyst for the Hydrogen Evolution Reaction. *Energy & Environmental Science* **2014**, *7* (8), 2624–2629.

(47) Xu, H.; Reunchan, P.; Ouyang, S.; Tong, H.; Umezawa, N.; Kako, T.; Ye, J. Anatase TiO2 Single Crystals Exposed with High-Reactive {111} Facets toward Efficient H2 Evolution. *Chemistry of Materials* **2013**, *25* (3), 405–411.

(48) Li, R.; Zhang, F.; Wang, D.; Yang, J.; Li, M.; Zhu, J.; Zhou, X.; Han, H.; Li, C. Spatial Separation of Photogenerated Electrons and Holes among {010} and {110} Crystal Facets of BiVO4. *Nature Communications 2013 4:1* **2013**, *4* (1), 1–7.

(49) Sun, S.; He, L.; Yang, M.; Cui, J.; Liang, S. Facet Junction Engineering for Photocatalysis: A Comprehensive Review on Elementary Knowledge, Facet-Synergistic Mechanisms, Functional Modifications, and Future Perspectives. *Advanced Functional Materials* **2022**, *32* (1), 2106982.

(50) Wang, X.; Wu, H. F.; Kuang, Q.; Huang, R. bin; Xie, Z. X.; Zheng, L. S. Shape-Dependent Antibacterial Activities of Ag2O Polyhedral Particles. *Langmuir* **2010**, *26* (4), 2774–2778.

(51) Wang, Y.; He, J.; Liu, C.; Chong, W. H.; Chen, H. Thermodynamics versus Kinetics in Nanosynthesis. *Angewandte Chemie International Edition* **2015**, *54* (7), 2022–2051.

(52) Kuang, Q.; Wang, X.; Jiang, Z.; Xie, Z.; Zheng, L. High-Energy-Surface Engineered Metal Oxide Micro- and Nanocrystallites and Their Applications. *Accounts of Chemical Research* **2014**, *47* (2), 308–318.

(53) Campisi, S.; Schiavoni, M.; Chan-Thaw, C. E.; Villa, A. Untangling the Role of the Capping Agent in Nanocatalysis: Recent Advances and Perspectives. *Catalysts 2016, Vol. 6, Page 185* **2016**, *6* (12), 185.

(54) Restrepo, C. V.; Villa, C. C. Synthesis of Silver Nanoparticles, Influence of Capping Agents, and Dependence on Size and Shape: A Review. *Environmental Nanotechnology, Monitoring & Management* **2021**, *15*, 100428.

(55) Shi, Y.; Lyu, Z.; Cao, Z.; Xie, M.; Xia, Y. How to Remove the Capping Agent from Pd Nanocubes without Destructing Their Surface Structure for the Maximization of Catalytic Activity? *Angewandte Chemie International Edition* **2020**, *59* (43), 19129–19135.

(56)   Kumazaki, Y.; Matsumoto, S.; Sato, T.; Tai, H.; Chang, P.-C.; Ho, H.-W. Anisotropic Etching of Si. *Journal of Micromechanics and Microengineering* **2019**, *29* (9), 093002.

(57)   Mulvihill, M. J.; Ling, X. Y.; Henzie, J.; Yang, P. Anisotropic Etching of Silver Nanoparticles for Plasmonic Structures Capable of Single-Particle SERS. *J Am Chem Soc* **2010**, *132* (1), 268–274.

(58)   Wang, S.; Liu, G.; Wang, L. Crystal Facet Engineering of Photoelectrodes for Photoelectrochemical Water Splitting. *Chemical Reviews* **2019**, *119* (8), 5192–5247.

(59)   West, A. *Solid State Chemistry and Its Applications, 2nd Edition, Student Edition*; Wiley, 2014.

(60)   Low, J.; Yu, J.; Jaroniec, M.; Wageh, S.; Al-Ghamdi, A. A. Heterojunction Photocatalysts. *Advanced Materials* **2017**, *29* (20).

(61)   Wu, N. Plasmonic Metal-Semiconductor Photocatalysts and Photoelectrochemical Cells: A Review. *Nanoscale* **2018**, *10* (6), 2679–2696.

(62)   Dutta, S. K.; Mehetor, S. K.; Pradhan, N. Metal Semiconductor Heterostructures for Photocatalytic Conversion of Light Energy. *Journal of Physical Chemistry Letters* **2015**, *6* (6), 936–944.

(63)   Abouelela, M. M.; Kawamura, G.; Matsuda, A. A Review on Plasmonic Nanoparticle-Semiconductor Photocatalysts for Water Splitting. *Journal of Cleaner Production* **2021**, *294*, 126200.

(64)   Liu, Z.; Hou, W.; Pavaskar, P.; Aykol, M.; Cronin, S. B. Plasmon Resonant Enhancement of Photocatalytic Water Splitting under Visible Illumination. *Nano Letters* **2011**, *11* (3), 1111–1116.

(65)   Liang, Q.; Liu, X.; Wang, J.; Liu, Y.; Liu, Z.; Tang, L.; Shao, B.; Zhang, W.; Gong, S.; Cheng, M.; He, Q.; Feng, C. In-Situ Self-Assembly Construction of Hollow Tubular g-C3N4 Isotype Heterojunction for Enhanced Visible-Light Photocatalysis: Experiments and Theories. *Journal of Hazardous Materials* **2021**, *401*, 123355.

(66)   Lu, N.; Jing, X.; Zhang, J.; Zhang, P.; Qiao, Q.; Zhang, Z. Photo-Assisted Self-Assembly Synthesis of All 2D-Layered Heterojunction Photocatalysts with Long-

Range Spatial Separation of Charge-Carriers toward Photocatalytic Redox Reactions. *Chemical Engineering Journal* **2022**, *431*, 134001.

(67)   Guo, C.; Wu, B.; Ye, S.; Liu, J.; Deng, X.; Luo, L.; Li, Q.; Xiao, X.; Wang, J.; Liu, J.; Xia, T.; Jiang, B. Enhancing the Heterojunction Component-Interaction by in-Situ Hydrothermal Growth toward Photocatalytic Hydrogen Evolution. *Journal of Colloid and Interface Science* **2022**, *614*, 367–377.

(68)   Bai, S.; Qiao, R.; Li, Z.; Xie, M.; Kong, Q.; Jiang, W.; Jiang, J.; Xiong, Y.; Bai, S.; Xie, M.; Kong, Q.; Jiang, W.; Qiao, R.; Li, Z.; Jiang, J.; Xiong, Y. Incorporation of Pd into Pt Co-Catalysts toward Enhanced Photocatalytic Water Splitting. *Particle & Particle Systems Characterization* **2016**, *33* (8), 506–511.

(69)   Gupta, S. M.; Tripathi, M. A Review on the Synthesis of TiO 2 Nanoparticles by Solution Route. *Central European Journal of Chemistry* **2012**, *10* (2), 279–294.

(70)   Radi, A.; Pradhan, D.; Sohn, Y.; Leung, K. T. Nanoscale Shape and Size Control of Cubic, Cuboctahedral, and Octahedral Cu-Cu2O Core-Shell Nanoparticles on Si(100) by One-Step, Templateless, Capping-Agent-Free Electrodeposition. *ACS Nano* **2010**, *4* (3), 1553–1560.

(71)   Jiang, J.; Zhao, K.; Xiao, X.; Zhang, L. Synthesis and Facet-Dependent Photoreactivity of BiOCl Single-Crystalline Nanosheets. *J Am Chem Soc* **2012**, *134* (10), 4473–4476.

(72)   Seifner, M. S.; Snellman, M.; Makgae, O. A.; Kumar, K.; Jacobsson, D.; Ek, M.; Deppert, K.; Messing, M. E.; Dick, K. A. Interface Dynamics in Ag–Cu 3 P Nanoparticle Heterostructures. *J Am Chem Soc* **2022**, *144* (1), 248–258.

(73)   El-Refaei, S. M.; Russo, P. A.; Pinna, N. Recent Advances in Multimetal and Doped Transition-Metal Phosphides for the Hydrogen Evolution Reaction at Different PH Values. *ACS Applied Materials and Interfaces* **2021**, *13* (19), 22077–22097.

(74)   Guo, X.; Cao, J.; Guo, M.; Lin, H.; Chen, Y.; Chen, S. Excellent Visible Light Photocatalytic H2 Evolution Activity of Novel Noble-Metal-Free Ni12P5/CdS Composite. *Catalysis Communications* **2019**, *119*, 176–179.

(75) Liu, J.; Li, Y.; Zhou, X.; Jiang, H.; Yang, H. G.; Li, C. Positively Charged Pt-Based Cocatalysts: An Orientation for Achieving Efficient Photocatalytic Water Splitting. *Journal of Materials Chemistry A* **2019**, *8* (1), 17–26.

(76) Gao, F.; Zhang, Y.; Wu, Z.; You, H.; Du, Y. Universal Strategies to Multi-Dimensional Noble-Metal-Based Catalysts for Electrocatalysis. *Coordination Chemistry Reviews* **2021**, *436*, 213825.

(77) Hong, L. Fei; Guo, R. Tang; Yuan, Y.; Ji, X. Yin; Lin, Z. Dong; Li, Z. Sheng; Pan, W. Guo. Recent Progress of Transition Metal Phosphides for Photocatalytic Hydrogen Evolution. *ChemSusChem* **2021**, *14* (2), 539–557.

(78) Yang, Y.; Zhou, C.; Wang, W.; Xiong, W.; Zeng, G.; Huang, D.; Zhang, C.; Song, B.; Xue, W.; Li, X.; Wang, Z.; He, D.; Luo, H.; Ouyang, Z. Recent Advances in Application of Transition Metal Phosphides for Photocatalytic Hydrogen Production. *Chemical Engineering Journal* **2021**, *405*, 126547.

(79) Su, J.; Zhou, J.; Wang, L.; Liu, C.; Chen, Y. Synthesis and Application of Transition Metal Phosphides as Electrocatalyst for Water Splitting. *Science Bulletin* **2017**, *62* (9), 633–644.

(80) Callejas, J. F.; Read, C. G.; Roske, C. W.; Lewis, N. S.; Schaak, R. E. Synthesis, Characterization, and Properties of Metal Phosphide Catalysts for the Hydrogen-Evolution Reaction. *Chemistry of Materials* **2016**, *28* (17), 6017–6044.

(81) Weng, C. C.; Ren, J. T.; Yuan, Z. Y. Transition Metal Phosphide-Based Materials for Efficient Electrochemical Hydrogen Evolution: A Critical Review. *ChemSusChem* **2020**, *13* (13), 3357–3375.

(82) Theerthagiri, J.; Murthy, A. P.; Lee, S. J.; Karuppasamy, K.; Arumugam, S. R.; Yu, Y.; Hanafiah, M. M.; Kim, H. S.; Mittal, V.; Choi, M. Y. Recent Progress on Synthetic Strategies and Applications of Transition Metal Phosphides in Energy Storage and Conversion. *Ceramics International* **2021**, *47* (4), 4404–4425.

(83) Carenco, S.; Portehault, D.; Boissière, C.; Mézailles, N.; Sanchez, C. Nanoscaled Metal Borides and Phosphides: Recent Developments and Perspectives. *Chemical Reviews* **2013**, *113* (10), 7981–8065.

(84)   Laursen, A. B.; Patraju, K. R.; Whitaker, M. J.; Retuerto, M.; Sarkar, T.; Yao, N.; Ramanujachary, K. v.; Greenblatt, M.; Dismukes, G. C. Nanocrystalline Ni5P4: A Hydrogen Evolution Electrocatalyst of Exceptional Efficiency in Both Alkaline and Acidic Media. *Energy & Environmental Science* **2015**, *8* (3), 1027–1034.

(85)   Pan, Y.; Liu, Y.; Zhao, J.; Yang, K.; Liang, J.; Liu, D.; Hu, W.; Liu, D.; Liu, Y.; Liu, C. Monodispersed Nickel Phosphide Nanocrystals with Different Phases: Synthesis, Characterization and Electrocatalytic Properties for Hydrogen Evolution. *Journal of Materials Chemistry A* **2014**, *3* (4), 1656–1665.

(86)   Callejas, J. F.; Read, C. G.; Popczun, E. J.; McEnaney, J. M.; Schaak, R. E. Nanostructured Co2P Electrocatalyst for the Hydrogen Evolution Reaction and Direct Comparison with Morphologically Equivalent CoP. *Chemistry of Materials* **2015**, *27* (10), 3769–3774.

(87)   Shi, Y.; Zhang, B. Recent Advances in Transition Metal Phosphide Nanomaterials: Synthesis and Applications in Hydrogen Evolution Reaction. *Chemical Society Reviews* **2016**, *45* (6), 1529–1541.

(88)   Weng, C. C.; Ren, J. T.; Yuan, Z. Y. Transition Metal Phosphide-Based Materials for Efficient Electrochemical Hydrogen Evolution: A Critical Review. *ChemSusChem* **2020**, *13* (13), 3357–3375.

(89)   Shi, Y.; Li, M.; Yu, Y.; Zhang, B. Recent Advances in Nanostructured Transition Metal Phosphides: Synthesis and Energy-Related Applications. *Energy & Environmental Science* **2020**, *13* (12), 4564–4582.

(90)   Kucernak, A. R. J.; Naranammalpuram Sundaram, V. N. Nickel Phosphide: The Effect of Phosphorus Content on Hydrogen Evolution Activity and Corrosion Resistance in Acidic Medium. *Journal of Materials Chemistry A* **2014**, *2* (41), 17435–17445.

(91)   Jiang, P.; Liu, Q.; Sun, X. NiP 2 Nanosheet Arrays Supported on Carbon Cloth: An Efficient 3D Hydrogen Evolution Cathode in Both Acidic and Alkaline Solutions. *Nanoscale* **2014**, *6* (22), 13440–13445.

(92) Huang, L.; Gao, R.; Xiong, L.; Devaraji, P.; Chen, W.; Li, X.; Mao, L. Two Dimensional Ni 2 P/CdS Photocatalyst for Boosting Hydrogen Production under Visible Light Irradiation. *RSC Advances* **2021**, *11* (20), 12153–12161.

(93) Dutta, A.; Dutta, S. K.; Mehetor, S. K.; Mondal, I.; Pal, U.; Pradhan, N. Oriented Attachments and Formation of Ring-on-Disk Heterostructure Au-Cu3P Photocatalysts. *Chemistry of Materials* **2016**, *28* (6), 1872–1878.

(94) Zhu, J.; Jiang, E.; Wang, X.; Pan, Z.; Xu, X.; Ma, S.; Kang Shen, P.; Pan, L.; Eguchi, M.; Nanjundan, A. K.; Shapter, J.; Yamauchi, Y. Gram-Scale Production of Cu3P-Cu2O Janus Nanoparticles into Nitrogen and Phosphorous Doped Porous Carbon Framework as Bifunctional Electrocatalysts for Overall Water Splitting. *Chemical Engineering Journal* **2022**, *427*, 130946.

(95) Bertoni, G.; Ramasse, Q.; Brescia, R.; de Trizio, L.; de Donato, F.; Manna, L. Direct Quantification of Cu Vacancies and Spatial Localization of Surface Plasmon Resonances in Copper Phosphide Nanocrystals. *ACS Materials Letters* **2019**, *1* (6), 665–670.

(96) Manna, G.; Bose, R.; Pradhan, N. Semiconducting and Plasmonic Copper Phosphide Platelets. *Angewandte Chemie* **2013**, *125* (26), 6894–6898.

(97) Wang, Q.; Xiao, L.; Liu, X.; Sun, X.; Wang, J.; Du, H. Special Z-Scheme Cu3P/TiO2 Hetero-Junction for Efficient Photocatalytic Hydrogen Evolution from Water. *Journal of Alloys and Compounds* **2022**, *894*, 162331.

(98) Snellman, M.; Eom, N.; Ek, M.; Messing, M. E.; Deppert, K. Continuous Gas-Phase Synthesis of Core–Shell Nanoparticles via Surface Segregation. *Nanoscale Advances* **2021**, *3* (11), 3041–3052.

(99) Zhang, Y.; Zuo, T. T.; Tang, Z.; Gao, M. C.; Dahmen, K. A.; Liaw, P. K.; Lu, Z. P. Microstructures and Properties of High-Entropy Alloys. *Progress in Materials Science* **2014**, *61*, 1–93.

(100) Britvin, S. N.; Murashko, M. N.; Vapnik, Y.; Polekhovsky, Y. S.; Krivovichev, S. v.; Vereshchagin, O. S.; Shilovskikh, V. v.; Vlasenko, N. S.; Krzhizhanovskaya, M. G.

Halamishite, Ni5P4, a New Terrestrial Phosphide in the Ni–P System. *Physics and Chemistry of Minerals* **2020**, *47* (1), 1–7.

(101) Olofsson, O. The Crystal Structure of Cu3P. *Acta Chemica Scandinavica* **1972**, *26* (7), 2777–2787.

(102) Frøseth, A. G.; Derlet, P. M.; van Swygenhoven, H. Twinning in Nanocrystalline Fcc Metals. *Advanced Engineering Materials* **2005**, *7* (1–2), 16–20.

(103) Rouquette, J.; Haines, J.; Fraysse, G.; Al-Zein, A.; Bornand, V.; Pintard, M.; Papet, P.; Hull, S.; Gorelli, F. A. High-Pressure Structural and Vibrational Study of PbZr 0.40Ti0.60O3. *Inorganic Chemistry* **2008**, *47* (21), 9898–9904.

(104) Khort, A.; Roslyakov, S.; Loginov, P. Solution Combustion Synthesis of Single-Phase Bimetallic Nanomaterials. *Nano-Structures & Nano-Objects* **2021**, *26*, 100727.

(105) Oryshchyn, S.; Babizhetskyy, V.; Zhak, O.; Stoyko, S.; Guérin, R.; Simon, A. Crystal Structure of HT-Ni5P2 and Reinvestigation of Isotypic Ni5As2. *Intermetallics (Barking)* **2011**, *19* (7), 1041–1046.

(106) Olofsson, O. The Crystal Structure of CuP2 and AgP2 with Some Phase Analytical Data of the Cu-P and Ag-P Systems. *Acta Chemica Scandinavica* **1965**, *19* (1), 229–241.

(107) Reyes-Gasga, J.; Gómez-Rodríguez, A.; Gao, X.; José-Yacamán, M. On the Interpretation of the Forbidden Spots Observed in the Electron Diffraction Patterns of Flat Au Triangular Nanoparticles. *Ultramicroscopy* **2008**, *108* (9), 929–936.
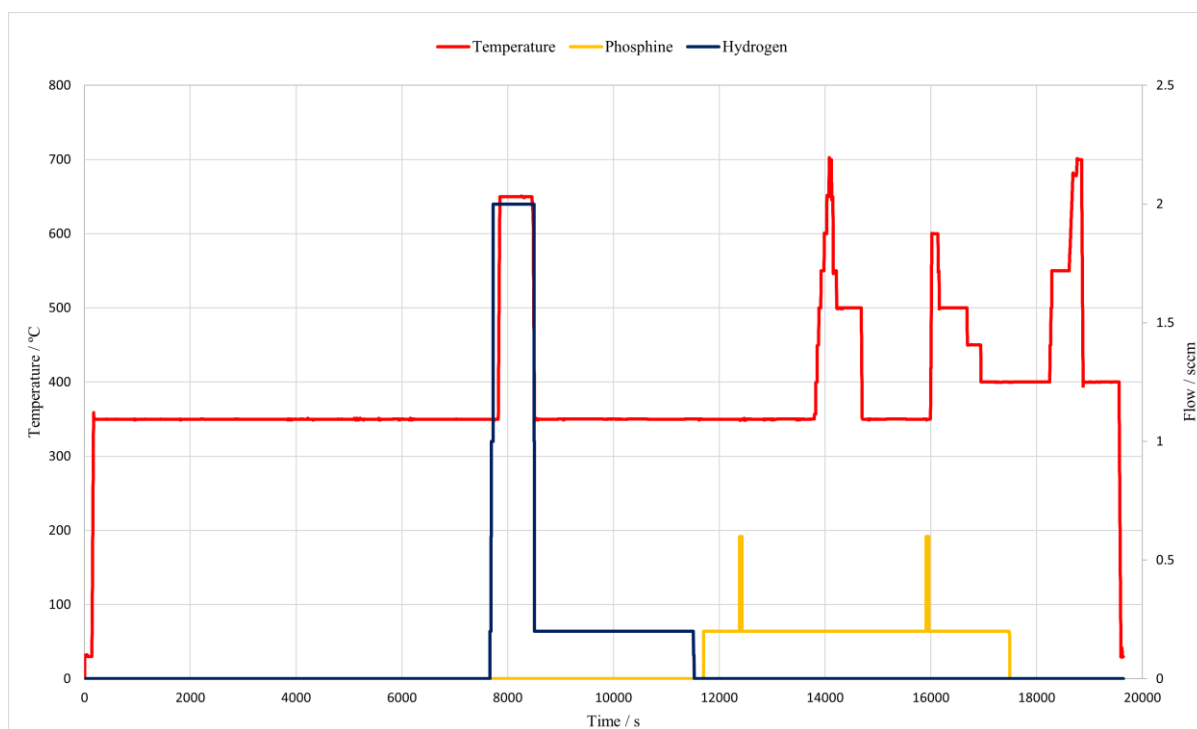
7   Appendix

Figure A. Detailed graph representing the process parameters of experiment 1. The annealing was performed at 650 ℃ with 2 sccm of H_2 for 12 min. In this experiment, 0.2 sccm of PH_3 were used for the initial reaction.
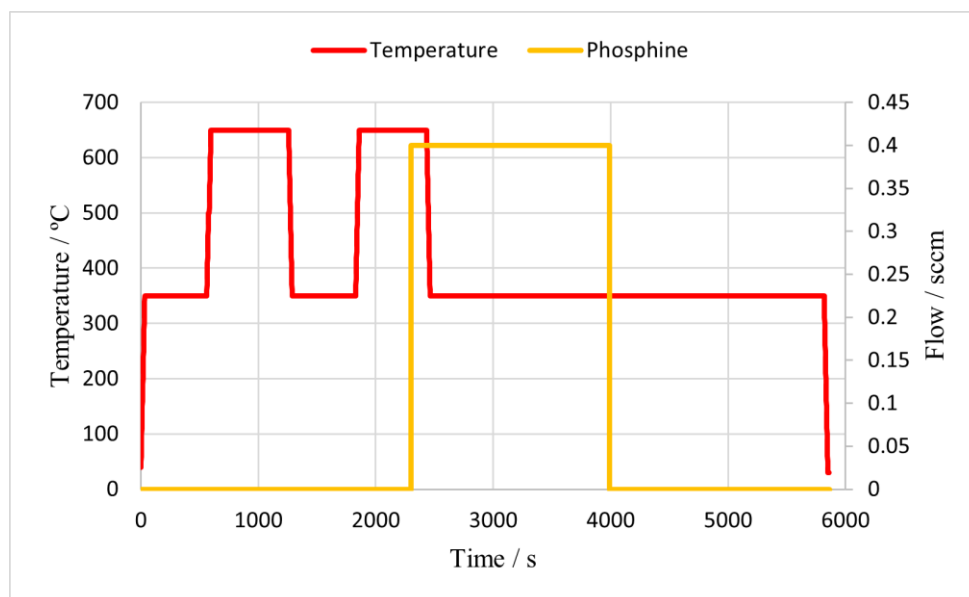

Figure B. Detailed graph representing the process parameters of experiment 2. In this experiment, no H_2 was used for the annealing. Two temperature annealings at 650 ℃ were performed for 12 and 10 min. The chemical reaction with the bimetallic NPs was performed with a flow of 0.4 sccm PH_3.
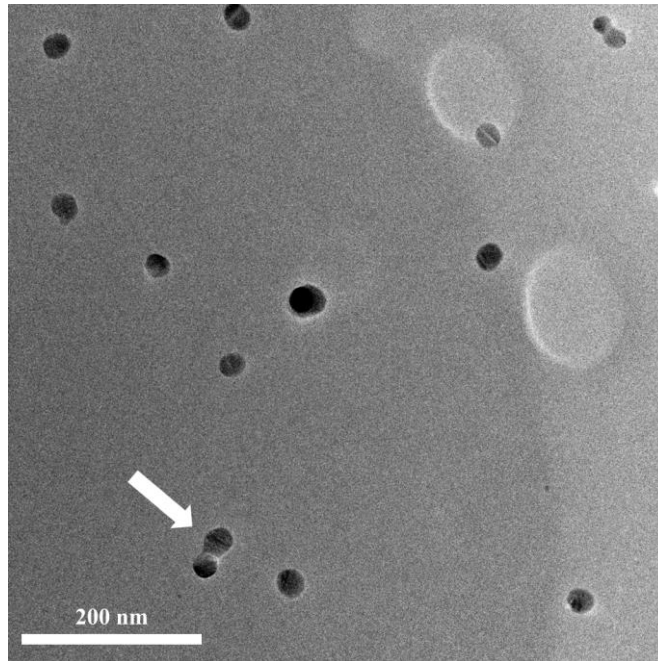
Figure C. HRTEM image of the generated Ni-Cu NPs by the spark ablation system. Most of the NPs have a diameter of approximately 30 nm. The NP indicated by a white arrow corresponds to the NP in Figure 4 and represents incomplete compaction observed for some agglomerates passing the furnace of the spark ablation system.
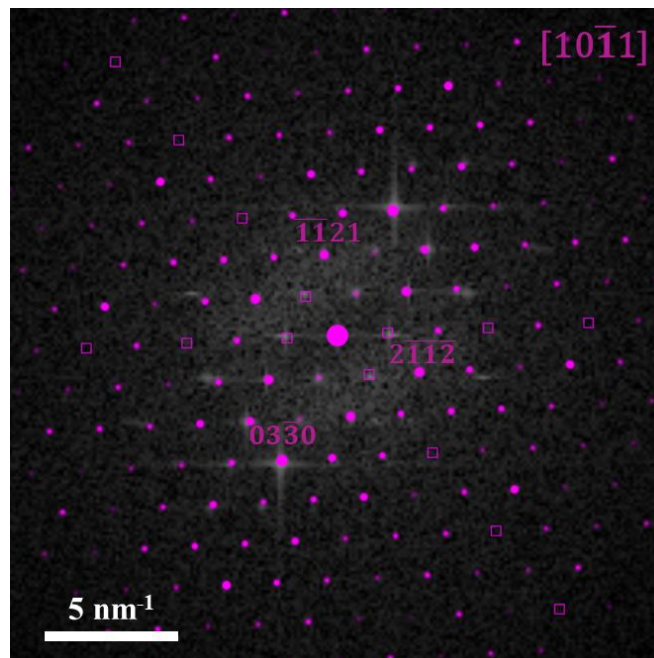

Figure D. Power spectrum of the HRTEM image in Figure 4b with overlaid simulated electron diffraction pattern of the $(Ni, Cu)_5As_2$ phase ([$10\bar{1}1$] zone axis, purple pattern). The overlaid squares represent forbidden reflections, which can be observed most likely due to the thin thickness of the crystal.[107]
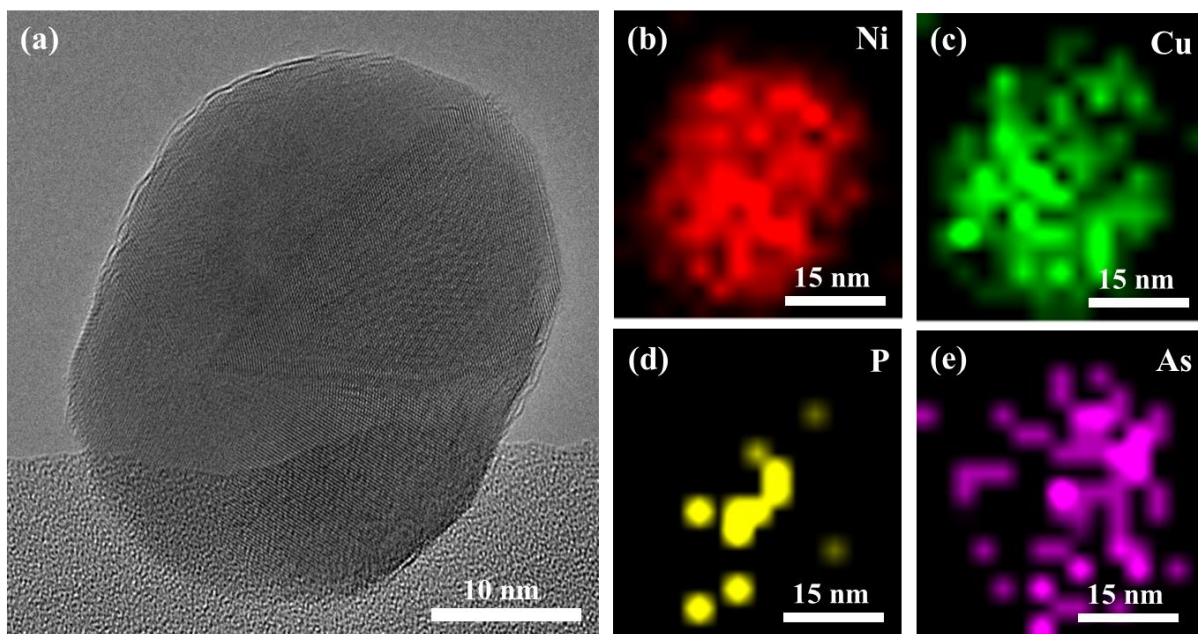
Figure E. (a) HRTEM image of a Ni-Cu NP with As contamination acquired at 350 ℃ without previous H_2 treatment and precursor supply. STEM-EDS elemental maps of (b) Ni ($K\alpha_1$), (c) Cu ($K\alpha_1$), (d) P ($K\alpha_1$), and (e) As ($K\alpha_1$) show the elemental distribution in the NP revealed in (a).